Estimation of Hourly Solar Loads on the Surfaces of Moving Refrigerated Tractor Trailers Outfitted with Phase Change Materials (PCMs) for Several Routes across the Continental U.S.

By

Krupasagar Varadarajan

B.E. ME, Anna University, Chennai, India, 2006

Submitted to the graduate degree program in the Department of Mechanical Engineering and the Graduate Faculty of the University of Kansas in partial fulfillment of the requirements for the degree of Master of Science in Mechanical Engineering

_____
Mario. A. Medina, Ph.D., P.E., Chairperson

_____
Bedru Yimer, Ph.D., Committee Member

_____
Terry Faddis, D.E., Committee Member

Date Defended: _____

The Thesis Committee for Krupasagar Varadarajan
Certifies that this is the approved version of the following thesis:

Estimation of Hourly Solar Loads on the Surfaces of Moving Refrigerated Tractor Trailers Outfitted with Phase Change Materials (PCMs) for Several Routes across the Continental U.S.

_____
Mario. A. Medina, Ph.D., P.E., Chairperson

Date approved:

Abstract

The primary objective of this thesis was to calculate solar loads, wind chill temperatures on the surfaces of moving refrigerated tractor trailers outfitted with phase change materials (PCMs) for several routes across the Continental United States. The second objective was to calculate hourly heat balances with more emphasis on the estimation of interior surface temperatures. PCMs have been widely tested and used in buildings during the past decades. As food transportation vehicles, experience different environmental conditions as they are in motion, the study of PCMs on food transportation vehicles could lead to new findings related to energy conservation. In this research work, a solar model was developed based on synthesized weather data files obtained from the National Solar Radiation Data Base (NSRDB), which contains weather information from 1961 through 1990 for 239 locations (TMY2 data) and weather information from 1991 through 2005 for 1020 locations (TMY3 data). The solar model was comprised of two parts, data extraction and solar load calculations. The data extraction part extracted the required fields from the TMY data and used them in the solar load calculations program to estimate the solar loads, wind chill temperatures and the interior surface temperatures of every exposed surface of a moving tractor trailer. These solar loads, wind chill temperatures and the interior surface temperatures would then be used in selecting the adequate type of PCMs for a particular route and time of year and to know, if the temperature where the PCMs will be placed will be "hot enough" to melt the PCMs and/or "cold enough" to solidify the PCMs. This is the case because PCMs are chosen, among other parameters, based on melting and solidification temperatures. In addition, the selection should also consider the construction of the truck, type of goods transported, indoor temperature of the truck’s refrigerated compartment and the PCM placement on the walls. The results obtained by incorporating PCMs in standard trailer walls, showed that

an average reduction in peak heat transfer rate of 29.1%, based on all surfaces (i.e., south, east, north, and west walls and the top surface), could be achieved. Overall average daily heat transfer reductions of 16.3% were observed in experiments of stationary standard trailer walls outfitted with PCMs. In conventional cargo trucks, the refrigeration unit is operated by burning fossil fuels, mainly diesel. Therefore, a decrease in refrigeration load, would have an impact in fuel consumption and in the reduction in size of the refrigeration equipment's.

Acknowledgements

I would like to take this opportunity to thank all who supported this academic aspiration. Firstly, I am indebted to Dr. Mario Medina, my thesis advisor, who supported me all the way in my Master's degree. I have been enormously benefited not only by his academic supervision but also the research assistantship that he provided me to explore and delve such great research experience. The professional ethics and academic teachings that I've learnt from him will be an asset all through my life. It is great honor to be his student. I would like to express gratitude to Dr. Bedru Yimer for supporting me with various issues during my graduate studies and being a graduate thesis committee member. I am also grateful to Dr. Terry Fadiis for willing to be a committee member of my graduate thesis.

I am very thankful to my co-researchers Ahmed and Meade for their valuable inputs and constant support. I would like to thank El Lee, Joseph Rendall, and Jin Xing, for their assistance with the research.

It is always a pleasure to remember my family, who has supported and encouraged me all through my life. My ardent respect goes to my parents and my brother who have been the motivation for all my achievements.

Last but not least, I would like to thank all my relatives and friends who are near and far from me but encouraged me every time.

Table of Contents

List of Figures

List of Tables

Chapter I: Introduction and current state of the problem

1. A brief history of PCM research work done at the University of Kansas

Thermal storage is one of the prime concerns in industries, food transportation, residential and commercial buildings. Increase in electric power for refrigeration and air-conditioning during the last decades has motivated researchers to work on reducing energy consumption and to find efficient ways of using other forms of energy (e.g., solar energy) during the day time. For example, both commercial and residential buildings have peak demands of electrical energy during the afternoon of any day. One way to keep this electric demand to a more constant value constant value could be accomplished by using renewable sources and thermal energy storage, which could potentially be integrated into the overall cycle of energy conversion and energy utilization. One way in which this can be achieved is by using phase change materials (PCMs) together with insulation materials. The idea of incorporating phase change materials in buildings was introduced approximately 40 years ago. However, several reasons exist as to why the technology is still not well developed and accepted. Some of these reasons include problems with the integration of PCMs into the insulation systems, PCM flammability, and in some cases PCM corrosiveness.

Extensive research on PCMs in building insulation has been conducted at the University of Kansas. The research group at the University of Kansas has focused on finding ways to incorporate PCMs in the insulation of building walls. For example, King [1, 2] research focused on evaluating the thermal performance of PCMs in Structural Insulated Panels (SIPs) in field testing. For this, two identical test houses were built. One house had the PCMs embedded within the SIPs and the other house was used as a control. That is, this house's walls did not include PCMs. The main objective of King's research was to lower the peak heat flux that

occurs across building walls in the mid afternoon. The experimental results showed that the peak heat fluxes were reduced approximately 37% with a PCM loading of 10%. The peak heat fluxes were reduced 62% with a PCM loading of 20%. "Loading" in this case meant the amount of PCM used as a percentage of wall interior siding (i.e., wallboard) weight.

Zhang [3, 4] developed a thermally-enhanced frame wall that also reduced peak heat fluxes across the wall and produced energy savings. The thermally-enhanced frame walls encapsulated the PCM in copper pipes. This type of wall was referred to as Phase Change Frame Wall (PCFW). It was reported that in field tests the PCFWs, assisted in reducing the wall peak heat fluxes as much as 38%, when compared to a standard frame wall system. The average wall peak heat flux was reduced by 15% when the PCM loading was 10% and to 9% when the PCM loading was 20%. The meaning of "loading" here is similar to that of King's.

Evers [5] developed and laboratory-tested a kind of insulation that included PCMs and cellulose insulation. This system was designed to work for use in frame walls. Evers used three types of PCMs, namely, paraffin based, hydrated-salt based, and eutectic type. The paraffin-based PCM was commercially-known as RT27, the hydrated-salt-based PCM was commercially-known as TH29-F127, TH24 and the eutectic type was commercially known as SP25. The number after the two letter code stands for the melting point of the PCMs in °F(°C). All these PCMs were mixed with cellulose insulation; one at a time, and the mixed PCM-insulation was placed in the cavities of frame walls. Experimental results showed that the insulation mixed with the paraffin based PCM (RT27) reduced the average peak heat flux by 9.2% when the loading concentration was 20%. Evers used a dynamic wall simulator for the testing.

Fang [6] showed that in field experiments the peak heat flux was reduced by 21% when using the thermally-enhanced cellulose insulation with RT27 at a loading concentration of 30%. These results were validated using a numerical code developed also by Fang [6].

Reshmeen [7] worked on determining the optimum placement and thermal performance of a PCM thermal shield incorporated in the insulation of frame walls. The performance of the thermal shields was evaluated in the laboratory using a dynamic wall simulator. Reshmeen's results showed reductions in peak heat flux across the walls produced by the PCM thermal shields. The peak heat flux reductions were in the range of 20 to 25% for a PCM loading of 20% when the PCM-shield was placed next to the interior surface of the wall's wallboard. This interior surface faced the internal part of the wall cavity.

Ahmed and Meade [8] used RT-5 phase change materials in the walls of conventional refrigerated trucks. Two cargo truck simulators were built using identical construction materials, which were tested under stationary environmental conditions in the field. The primary objective of the research focused on the estimation of the peak heat flux and total heat flow behavior of the two units. The results suggested that the peak heat flux was reduced by 42.2% and total heat transfer in one day was reduced by 27.7%. Month-long result suggested that the peak heat flux was reduced by an average 43.8% and total heat transfer in one month was reduced by 26.3%.

From this research review section, it is evident that PCMs can potentially reduce heat fluxes and total heat transfer across walls of building and refrigerated trucks. As the earlier work by Ahmed and Meade used only stationary tractor trailers, the main focus work of this research was to develop computer models to study the performance of PCM-enhanced tractor trailer walls, while in motion. The first step towards this goal was to develop a solar model, which could be used to estimate external surface temperatures of a moving refrigerated truck cargo box.

This, in turn, would help in selecting the most adequate PCM for specific routes during the various seasons and weather variations. Also, this research would help in understanding PCM performance when integrated in moving systems, such as refrigerated tractor trailers. In addition, this solar model could be used in countries other than the U.S.

2. Energy consumption in the transportation sector by refrigerated trucks

The concept of food refrigeration started almost 150 years ago, where, in China, ice was first harvested and stored [10]. The Greeks and the people of what now is Israel used to place large amounts of snow in storage pits dug in the ground and insulated with wood [10]. Ancient Egyptians placed water on the roof, thus exposing it to night's cool air and sky radiation [10]. In the U.S., by 1799, ice was commercially transported from New York City to Charleston, S.C., but unfortunately not much of ice was left when it reached Charleston [10]. As the demand to transport food to different places increased, people started working on building more efficient refrigeration devices with finer tolerances.

During the mid-1800's, ice was shipped to tropical climatic regions in insulated containers, thus decreasing the melting of ice drastically [9]. In 1805, the American inventor Oliver Evans designed the first refrigeration machine that used vapor instead of water [9]. But it was the American physician John Gorrie who constructed the machine [9]. James Harrison an Australian, who examined the previous refrigeration devices, came up with a concept of vapor-compression refrigeration for meat and dairy-products [9].

During the 1840's refrigerated cars were used to transport dairy products [10]. In 1867 J.B. Sutherland patented the first refrigerated rail road car that used ice bunkers in each end [10]. The first refrigerated car to carry fresh fruit was built in 1867 by Parker Earle, of Illinois, who shipped strawberries using the Illinois Central Railroad [10]. But it was not until 1949 that refrigeration systems made it into the trucking industry by roof mounted cooling devices, patented by Fred Jones [10]. Vegetables cultivated and produced in western plains in the United States needed to be transported over long distances all over the country. The increase in agricultural output was a major contributor in the development of refrigerated trucks.

Refrigerated trucks helped the farmers transport their food products from rural areas to city markets efficiently. But the major factors that attracted farmers were speed and flexibility [16]. Refrigerated trucks allowed the farmers to expand their business beyond 50 or 100 miles (80 km or 160 km) where the produce was farmed [16]. In spite of reducing the energy intensity within the transportation sector over past few years, costs still remain high. In the United States, in 2005, trucks alone consumed about 65% of the total energy consumption by freight transportation [11]. To maintain the required temperature inside the refrigerated trucks, these require proper refrigeration units, which operate by burning fuel.

3. Challenges of refrigerated transportation

As the population continues to grow, the demand for food is also increasing. In the United States, nearly 85% percent of all energy is produced by burning fossil fuels [12]. One area responsible for the increase in fossil fuel burning is refrigerated trucks. A general estimate shows that 80% of communities across the United States receive their goods exclusively by trucks [13], of which a significant number are climate-controlled. Furthermore, they carry perishable goods, pharmaceutical items, and many other temperature-sensitive commodities. In the United States, a total of 787,000 trucks were registered in 1965, which consumed 6.7 billion gallons of fuel [14]. In 1997, nearly 1,790,000 trucks were registered, which consumed 20.3 billion gallons of fuel [14]. All these trucks transport climate-controlled goods throughout the United States. The most astonishing fact is that nearly 485,000 trucks leave California alone to transport fruit and vegetables to distances between 100 to 3100 miles (160 km or 4988 km) [15]. In 2005, nearly 120 billion of agricultural products crossed the United States border [16]. In 1981 about 50 percent of produce came by truck and 50 percent by rail. In 1998 about 87 percent of produce arriving at the Chicago terminal market from all locations came by truck, while rail accounted for about 13 percent [16]. The fuel consumption by truck industry, both light and heavy duty trucks, has tripled during the last three decades, resulting in approximately 6 million barrels of oil per day in 2005 [17]. The U.S. Department of Energy estimated that by end of 2030, trucks will consume around 11.5 million barrels of oil per day, which is half of the total consumption by all the transportation modes.

4. PCMs in refrigerated transportation

Phase Change Materials (PCMs) offer a solution for reducing fuel consumption in refrigerated trucks. PCMs store and release energy during melting and freezing (i.e., while changing from one phase to another). When PCMs melt they absorb a relatively large amount of heat energy in the form of latent heat of fusion. When PCMs solidify, the absorbed heat energy is released to the environment. For example as, it was shown in the previous sections, PCMs help in reducing electricity demand during the daytime either by absorbing heat or by storing heat energy.

Water is the cheapest phase change material available on earth, but its freezing temperature makes it ineffective for use in most thermal energy storage applications because water changes its states at both 32°F and 212°F (0°C and 100°C). There are different types of commercially-available phase change materials with wide range of melting and solidification temperatures that can be selected based on the application.

Recent developments in phase change materials show that these can be used in the walls of refrigerated trucks to reduce heat transfer, which in turn would help in reducing fuel consumption. Most of the refrigeration units used in refrigerated trucks operate by consuming liquid fuels, usually the same fluid used to operate the trucks. If the similarities and differences of the phase change materials are used in buildings and transportation are compared, it can be inferred that the applications are almost the identical with few differences, the most relevant being their melting point. The most commonly insulating material used in buildings are fiberglass, in its various forms, polyurethane foams, cellulose, and other foam products. In refrigerated trucks, polyurethane foams or other similar foams are sandwiched between aluminum, stainless steel or fiberglass boards. Furthermore heat transfer processes across the

walls of a building and the walls of an insulated refrigerated cargo truck trailers have many common features. In spite of all these similarities, the main difference between buildings and transportation is the state of motion. Buildings are static and stationary structures and trucks are ambulatory systems that experience changes in air motion and varying solar radiation. In addition trucks navigate into several types of environmental conditions as they travel long distances and cross latitudes and longitudes. The previous PCM research work in refrigerated trucks conducted at the University of Kansas was based on stationary condition [8], which is referred as engine idling. To take this research to the next level of practical implementation, it was necessary to study wind effects and solar radiation on various surfaces of the truck at various locations within the same traveling period. The current research focused on developing a solar model to estimate the solar loads and wind-chill temperatures on the various surfaces of a moving cargo truck trailer. This was done to identify the acceptable PCMs for specific routes.

Chapter II: PCM - Literature review

1. Introduction

Thermal energy storage is not the permanent storage of heat at high or low temperature, but rather the temporary storage of heat, which can be used at a later time to avoid the gap between energy production and energy used. The system design is based on storage requirements. The criteria used to select, or design, storage systems are as follows:

- **Reduced operating cost** – By having proper load shifting, the annual operating cost are reduced.
- **Reduced machine size** – The machine size is reduced to a greater extent by proper load shifting.
- **Increased capacity** – Thermal energy storage increases the system output without increasing the machine size.
- **Green solution** – CO_2 emissions are reduced by reduced machine size and annual energy consumption.

For latent heat storage systems to operate effectively in commercial and residential buildings, an acceptable choice of PCMs is required. PCMs are integrated into building ceilings, walls and floors for thermal energy storage. PCMs absorb solar energy directly or through natural convection when they melt. This thermal energy storage also increases human comfort by minimizing the swing in wall temperatures. As HVAC systems typically have longer "on" cycles; indoor air temperature and humidity are maintained closer to the desired temperature and humidity for longer periods of time. Latent heat storage offers a potential solution to reduce the gap between energy supply and demand.

By their name, PCMs suggest that they are materials that change phase as a result of temperature changes. The phase change temperature differs considerably between PCMs depending on their application. For example water freezes at 32℉ (0℃) and boils at 212 ℉ (100℃), while lauric acid, which is an organic PCM, freezes at 109℉ (43 ℃) and boils at 570 ℉ (299 ℃). When the ambient temperature of the PCM environment increases, PCMs changes from solid to liquid by absorbing heat from the surrounding environment. PCMs can absorb and store thermal energy to a significant degree in comparison to normal construction materials (through the process of latent heat).

2. Desired properties of PCMs

- PCMs should have high latent heat of fusion per unit mass, so that smaller quantities of material store more energy.
- PCMs should have high specific heat capacity to provide additional sensible heat storage effects and also to avoid subcooling (is the process by which a saturated liquid is cooled below the saturation temperature, forcing it to change its phase completely).
- PCMs should melt and freeze over small temperature ranges. PCMs should have high thermal conductivities so that the temperature gradient required for charging the storage material is small.
- PCMs should have high density; so that smaller containers would be needed.
- PCMs should be non-toxic, non-flammable, and non-explosive.
- PCMs should have an appropriate life span.
- PCMs should be compatible and non-corrosive to the holding material.
- PCMs should have a high nucleation rate to avoid supercooling and high crystal growth.
- PCMs should exhibit little or no supercooling (is the process of lowering the temperature of a liquid, below its freezing point without it becoming a solid) during freezing. Supercooling comes into play in salt hydrates and eutectic solutions. PCMs in its liquid state can be cooled below its freezing point and few salt hydrates can be cooled to 122°F (50°C) below its freezing point. But in most applications supercooling must be kept little or none by adding suitable nucleating (Nucleation is generally a physical reaction, which occurs when components in a solution start to precipitate out, forming nuclei which attract more precipitate) agents to the PCM.
- PCMs should have an acceptable price.

3. Classification of PCMs

PCMs are classified as follows:

- **Eutectics** – mixture of two or more components that solidifies at its minimum freezing point. For example, eutectic compositions are used for storage applications for temperatures temperature below $32°F\ (0℃)$ [18].
- **Salt hydrates –** All inorganic thermal salts are hydrated salt based PCMs, which consist of salt and water in discrete mixing ratios with stable crystal structures. Salt hydrates cover a temperature range between $41°F$ to $266°F\ (5℃$ to $130℃)$ [18].
- **Organic PCMs -** PCMs like paraffin, fatty acids, and sugar alcohols are organic PCMs whose application temperature range is between $32°F\ (0℃)$ and about $393°F\ (200℃)$ [18].

a. Inorganic PCMs:

Salt-hydrates are classified as inorganic PCMs. Salt hydrates consist of salt and water in a distinct mixing ratio [18] with an integral number of water molecules per ion pair of the salt and with a stable crystal structure. In salt hydrates, water molecules are located and oriented in the structure in a well-defined manner. Since salt hydrates consist of at least one water and one salt molecule, they separate into two phases, thus showing phase segregation. They exhibit excellent volumetric heat storage density $9393\ \mathrm{Btu/ft^3}(350\ \mathrm{MJ/m^3})$ [18], when compared to heat storage density with respect to mass. Inorganic materials cover a temperature range between $41°F$ and $266\ °F\ (5℃$ and $130℃)$ and show high thermal conductivity $0.35\ \mathrm{Btu/hr-ft-f}\ (0.2\ \mathrm{W/m\,K})$, when compared to other PCMs. Their safety and price varies according to the salts, but these are inexpensive when compared to paraffins. Inorganic PCMs melting enthalpy

increase roughly proportional to their melting temperature, so salt hydrates with high melting temperature exhibit high melting enthalpy. Nevertheless, all inorganic PCMs are corrosive and hygroscopic (is the ability of a substance to attract and hold water molecules from the surrounding environment through either absorption or adsorption) in nature. As a result of this, PCMs must be enclosed in special corrosion and water resistant containers. In almost all cases, salt hydrates are chemically stable. Certain disadvantages of inorganic PCMs are phase segregation and subcooling. Inorganic PCMs melt congruently with the formation of hydrated salt at the bottom, which results in a reduction in storage efficiency [18]. In order to overcome this many researchers suggested that the addition of extra water to prevent the formation of anhydrous salt [18]. The main disadvantage of adding water is that it reduces the storage capacity of the salt hydrates and the systems need to be operated with larger temperature swings. The other way of overcoming phase segregation is by adding thickening agents, but this reduces the rates of crystallization and heat transfer of the salt hydrates due to the thermal conductivity of the mixture.

b. Organic PCMs:

Organic PCMs are classified as paraffin and non-paraffin, with organic paraffin being the first choice over inorganic PCMs due to their lower price and chemical stability.

Paraffins:

The most commonly used organic PCM is paraffin wax. Paraffin is also referred as alkane. It has the general formula C_nH_{2n+2}. Commercially-available paraffin wax is made by the process of petroleum distillation. Paraffins exhibit good latent heat storage densities with respect to mass and melting and solidification take place with negligible subcooling. Paraffin wax is chemically inert and no phase segregation takes place. Organic PCMs usually have low melting enthalpy per

volume than inorganic PCMs and low latent heat of fusion, when compared to pure alkanes. These PCMs cover the temperature range between 32°F (0°C) and about 392°F (200°C) [18]. Pure paraffin waxes are expensive, and therefore, only technical grade paraffins can be used.

Non-paraffin:

Esters, fatty acids, alcohols, and glycols are non-paraffin PCMs. Low thermal conductivity is part of the organic PCMs. To overcome this non-paraffin metallic fillers are used to improve their conductivity and thermal diffusivity [18]. When non-paraffins are exposed to high temperatures, they ignite or oxidize thus becoming unstable and toxic. Investigators [19] analyzed the thermal properties of fatty acids and found that they are excellent for latent heat thermal storage in space heating applications. The melting range of the fatty acids varies in the range 86°F to 149°F (30°C to 65°C) [19].

c. Eutectics:

Eutectic compositions are combinations of two or more constituents, which have the ability to solidify simultaneously out of the liquid phase at a minimum freezing point, also called the eutectic point. At the eutectic point, the liquid phase reacts to the solid phase which is composed of two or more solid phases with different composition; however, the overall composition is still the same as in the liquid. Therefore, eutectic compositions do not show phase separation. Eutectics show both reliable melting and solidification behaviors, which results in a congruent crystallization processes with consistency in the crystalline composition. As a result of addition of salt, eutectic solutions exhibit melting temperatures below 32°F (0°C) [18] and have good storage densities. The effects of repeated thermal cycling in eutectic solutions does not reflect in supercooling and very rarely does the solid to liquid transition phase produce uneven liquidity in the mixture as a result of the strong chemical composition.

4. PCM – Encapsulation

i. Flat containers:

In recent times several companies have developed different PCM encapsulation methods. One such encapsulation is flat containers. Flat containers are made of blow molded high density polyurethane. These flat containers can be used for both low and high temperature range applications. When used for high temperature applications, the containers might soften. Each flat container can hold a sufficient amount of PCM and it can be easily stacked on top of one another in a bulk volume. The gaps between flat containers may be used to allow air or water to flow easily to provide sufficient heat exchange [20]. Figure 1 shows the flat container encapsulation.

Figure 1: Flat containers [20]

ii. Tubular containers:

Tubular containers are very similar to flat containers. These tubular containers are also made of high density polyurethane. The space between tubes can be used for air or water passage to allow excellent heat exchange properties [20]. Figure 2 shows a kind of tubular container encapsulation.

Figure 2: Tubular containers [20]

iii. Spherical containers

This type of encapsulation is used for positive temperature range. Once the PCM is incorporated into a plastic or rubber matrix, it is molded to produce standard sized balls or any shape. Spherical containers can be easily immersed in residential/commercial tanks for storing heat [20]. Figure 3 shows one kind of spherical container encapsulation.

Figure 3: Spherical containers [20]

iv. Eutectic system:

In Eutectic systems, the PCMs are filled in either hollow tubes or plates. PCMs in eutectic system can be charged during the night time using off peak electricity. Once the eutectic system has solidified, it can be used for providing refrigeration along with the mechanical refrigeration during the day time, thus reducing the peak energy consumption [20]. Figure 4 shows an eutectic system used in a truck for food transportation.

Figure 4: Eutectic system [40]

v. PCM pouches:

One of the simplest ways of incorporating PCMs in buildings and transportation can be using small metallic or non-metallic pouches or bags. Reshmeen [7] effectively used plastic bags to encapsulate PCMs. To have the proper volume expansion, only a certain portion of each plastic bag needs to be filled. Figure 5 depicts an assortment of PCM pouches available in the market.

Figure 5: PCM pouches [20]

vi. Microcapsulated PCMs:

Some PCMs undergo significant changes from solid to liquid and vice versa. To remain functional over a high number of cycles, these PCMs must be microencapsulated and the PCMs must remain within the microcapsule for the whole lifespan. Holman [21] patented the first microencapsulated PCM consisting of a polymeric shell and a metal oxide gel with improved mechanical stress and flame resistance. Figure 6 shows the microencapsulated PCMs.

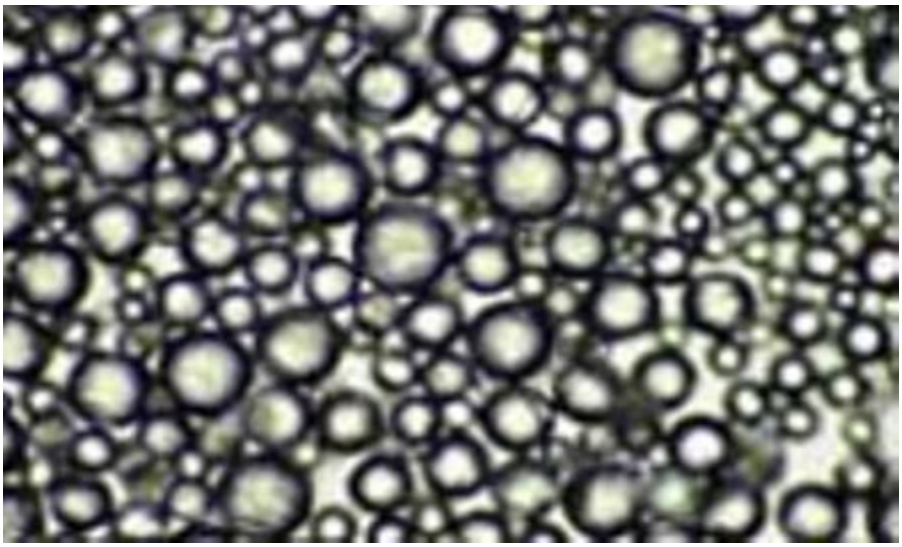

Figure 6: Microencapsulated PCMs [22]

5. PCM – Applications

i. Buildings:

PCMs use in buildings is an application widely studied for reducing space heat and cooling energy use in buildings [23]. The application of PCMs in buildings is acceptable, because it offers the potential to smooth wall temperature variations and it can be easily employed along with building construction materials, such as plasterboard and insulation products. In addition, to reduce solar gain in buildings, PCM curtains and PCM-shading system can be used for windows. The windows are generally fitted with two sheets of glass with a gap between them, which is filled with PCM.

ii. Back-up cooling systems:

Power failure in food storage facilities could have significant impact on the quality of the food products. In fact, PCMs are employed in warehouses, in case power delivery fails. That is, PCMs absorb heat from the warehouse during power failure to ensure that the products remain fresh.

iii. Eutectic systems:

Eutectic systems consist of hollow tube or plates filled with eutectic solutions of PCMs. Eutectic systems store energy and release it whenever required. The hollow tubes or plates filled with the eutectic solution are charged during night time and allowed to operate by providing sufficient cooling during the day time. Eutectic systems could be fitted in truck trailer along with the vapor compression systems. Eutectic systems can be effectively used during short trips, but there might be some heat gains resulting from the frequent opening of doors.

iv. Solar energy storage:

During summer time, the temperature of the heat transfer fluid from solar collector is in the range of 158 °F to 194 °F (70℃ to 90℃) and it can be used to heat hot water containers. In winter, the temperature of the heat transfer fluid is in the range of 95°F to 140°F (35℃ to 60℃) range. During this time solid-liquid PCMs can be used to store energy.

v. Road transport:

The majority of goods like vegetable, fruits, meat and medicines are transported by refrigerated trucks in the Continental United States. In many cases the product temperature should be controlled at certain temperatures. PCM technology offers the potential to help in storing heat, which can be used effectively as a temperature management tool [24].

vi. Automobiles:

When an automobile engine starts at lower temperature, energy needs are relatively high. To avoid this, modern vehicles use a heat storage system whereby a heat storage fluid is heated by engine coolants as the engines run. Whenever the engine is turned off, the heat stored can preheat the engine [24].

vii. Electronic components:

In general, electronic components tend to fail as result of increases in operating temperature as well as wear and tear. PCMs are used to help in restricting temperature rises in electronic components. Because PCMs act as passive components, they don't need any additional source of energy to operate [24].

Chapter III: Experimental setup

1. Setup

Two truck trailers simulators with a dimension of 48 in x 48 in x 48 in (1.22 m x 1.22 m x 1.22 m) were constructed with identical wall panels at the University of Kansas by Ahmed and Meade [8]. One of the truck trailer simulators was outfitted with PCMs through encapsulated pipes (herein referred to as PCM unit). The other truck trailer simulator had standard wall panels, but without PCM. This simulator is herein referred to as control unit. The small-scale trailer simulators are shown in Figure 7.

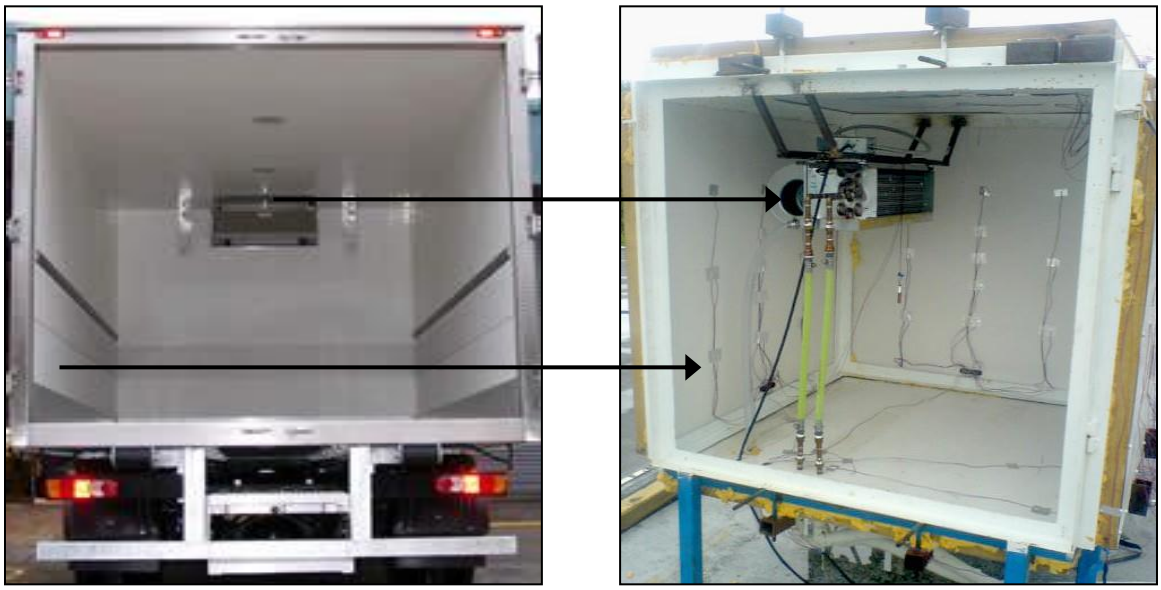

Figure 7: Trailer simulator and similarity between commercial and test trailer [8]

The collage of pictures shown in Figure 8 provides the progression of how the simulators were constructed.

Figure 8: Collage of pictures of the simulator construction; frame of the simulators (left), a panel before installation (right top) and complete simulators (right bottom) [8]

Once the walls were installed, foam sealant was used to leak proof the simulators. To facilitate the electrical wire connections to the simulators, three holes were drilled in the bottom panel. The truck simulators were placed side-by-side with enough distance to insure that shadow of one simulator did not fall on the other simulator. Both the simulators were strapped down to heavy cement blocks. An instrument shed was constructed to place all the cooling equipment, data acquisition system, computer, thermostat etc. and to protect them from inclement weather and hot sun. Figure 9 shows the entire setup on the rooftop of Learned Hall at the University of Kansas.

Figure 9: Experimental setup showing the two refrigerated trailer simulators, control shed, and refrigeration equipment [8]

2. Panel construction

The panels for the truck simulators were constructed in house based on guidelines from the trucking industry. The polyurethane foam insulation was sandwiched between aluminum and glass boards, which is the common practice in the truck industry. Table 1 shows the specifications of the panel construction. The basic difference between the two truck simulators was that one truck simulator had a standard walls and the other one was outfitted with half inch copper pipes, which contained PCMs. Figure 10 shows a section on the construction of the wall panels with the PCM pipes. The PCMs were encapsulated in eight copper pipes totaling 25% of the total insulation foam weight.

Extra care was taken to minimize the air intrusion during panel construction and to avoid the empty space between aluminum and glass board.

Table 1: Wall panel construction details [8]

Material	Thickness	Dimension
Aluminum	0.04 in (0.102 cm)	47 in × 47 in (119.4 cm × 119.4 cm)
Polyurethane foam	3.5 in (8.89 cm)	
Glass board	0.09 in (0.229 cm)	47 in × 47 in (119.4 cm × 119.4 cm)
Wood frame		2 in × 4 in (5.08 cm × 10.2 cm)
Copper pipe		0.5 in × 44 in (1.27 cm × 111.76 cm)

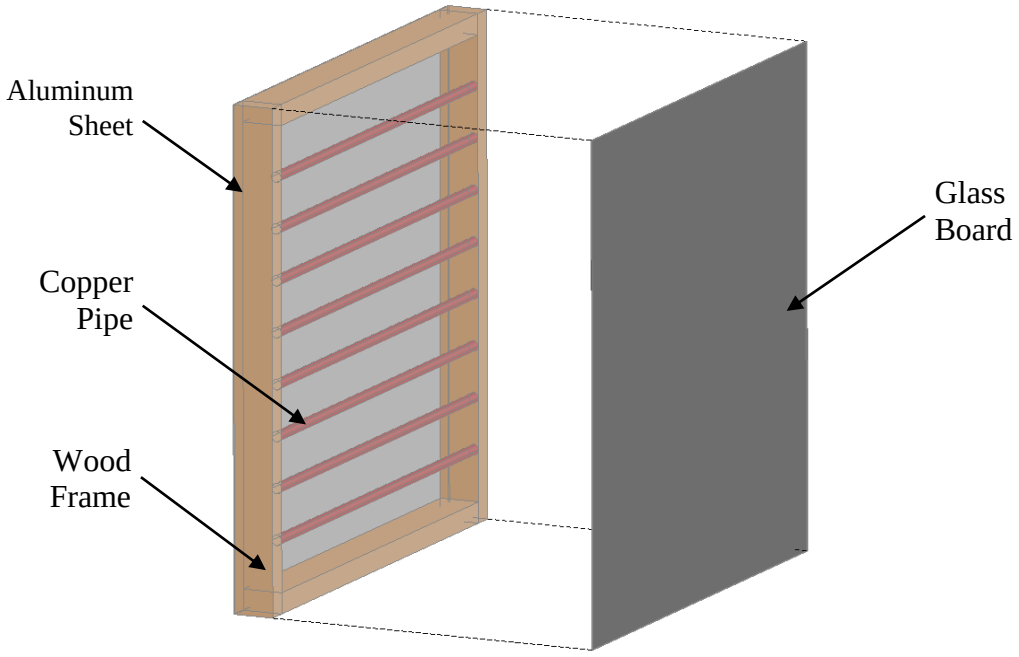

Figure 10: Cut-away view of a tractor trailer simulator wall with PCM pipes [8]

Figure 11 shows the polyurethane foam expanding within the contained space of the wall.

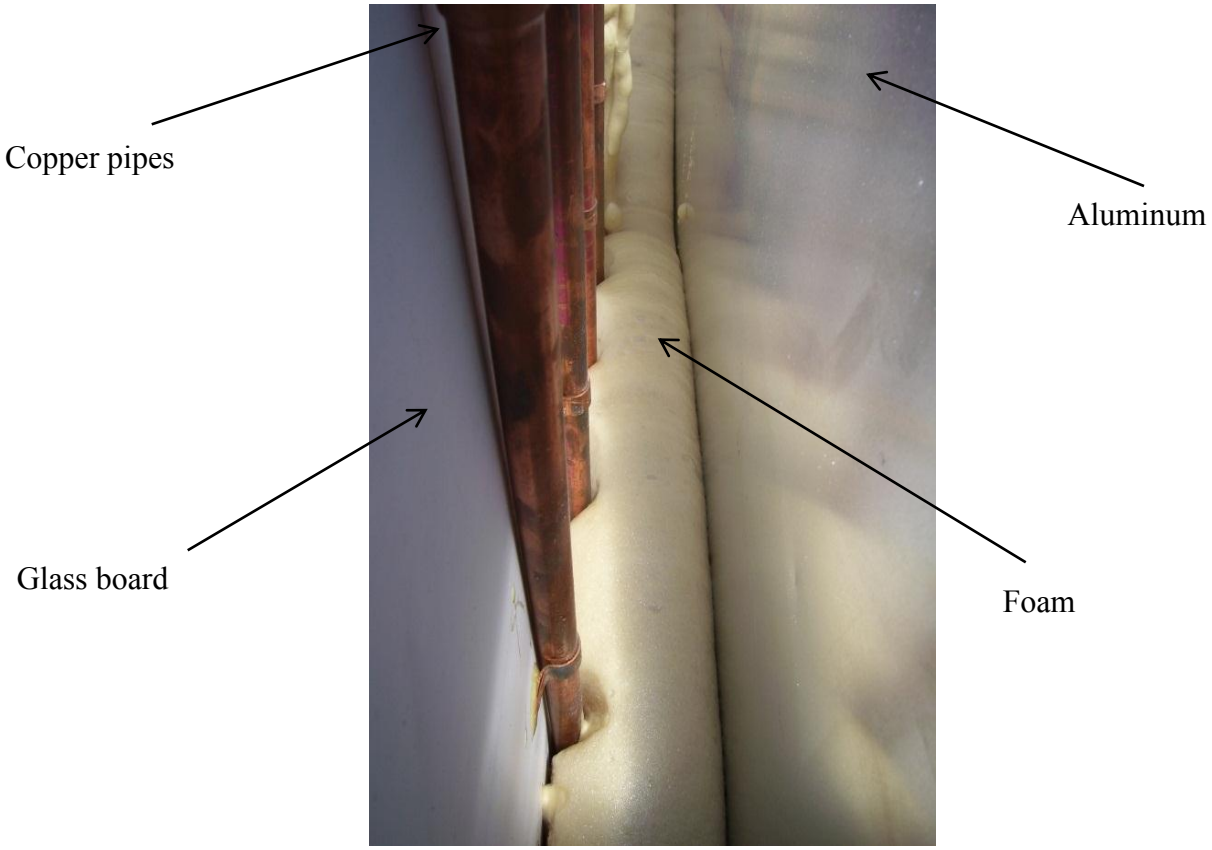

Figure 11: Inside look at the wall, while the polyurethane foam is expanding within the contained space of the wall [8].

The PCM pipes were placed at equal distances. Copper caps were used to seal the end of the PCM pipes. The PCM pipes were placed close to the indoor part of the wall to achieve better results.

3. Cooling circuit

The major challenge was to obtain the desired indoor temperature. To achieve this, Ahmed and Meade [8] designed and built a cooling unit to provide refrigeration. The cooling unit was a closed loop system, which consisted of a chiller, a pump, and two fan coil units. The inlet and outlet of the chiller were connected to the fan coil units. This enabled the coolant to flow through the chiller and then to the fan coil units and return to the chiller unit. A centrifugal pump with a capacity of ½ hp (0.37 kw) was used to facilitate a smooth flow of coolant.

Figures 12, 13 and 14, show a detailed view of the cooling system components. The chiller had a cooling capacity of 682 Btu/hr (200 watts) at $32°F$ $(0℃)$. The chiller unit was set to $23°F$ $(-5℃)$ to achieve the desired refrigeration inside the simulators. To prevent heat gains, the entire piping system was insulated. In addition to that, four axial fans with a capacity of 230 cfm (109 liters/sec) were added to the house unit to facilitate the air flow. This helped in maintaining a standard temperature in the equipment shed.

The cooling unit was divided into primary and secondary cooling loops. The primary cooling loop consisted of a chiller unit and the coolant flow in the circuit. The secondary cooling loop consisted of a pump and the fan coil units. Propylene glycol, an anti-freeze coolant was used to avoid any freezing problem within the circuit. The chiller unit was tuned to as low as $14°F$ $(-10℃)$ to achieve the desired temperature of $39°F$ $(4℃)$ in the simulator units.

Figures 12 and 13 show the schematic of the cooling circuit and the equipment housing.

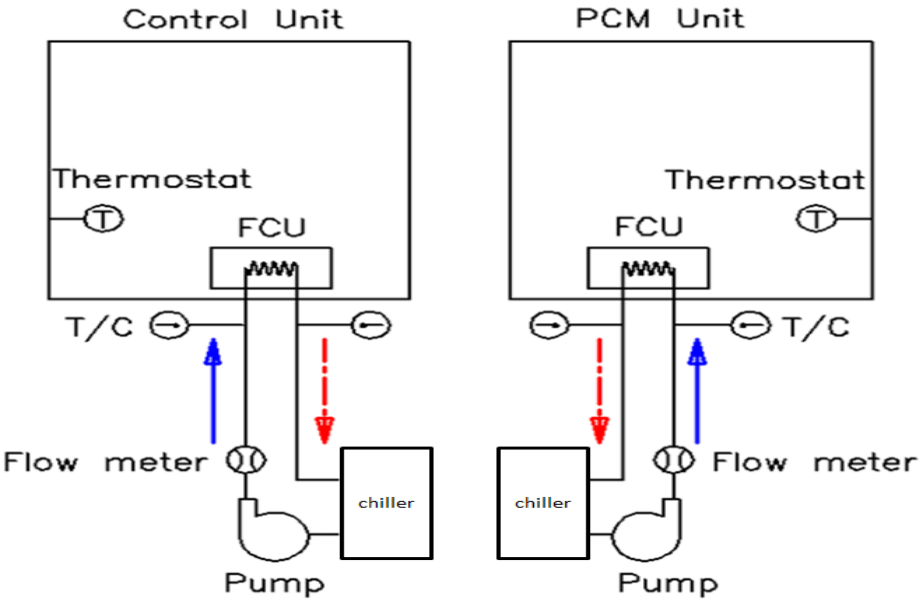

Figure 12: Schematic of the cooling circuit; solid arrows indicate coolant supply, dashed arrows represents coolant return [8]

Figure 13: Equipment house showing the chiller (front) and data logging equipment [8]

The fan coil unit shown in Figure 14 was the main cooling unit in the simulators.

Figure 14: Fan coil unit inside the simulator [8]

The capacity of fan coil units was 300 cfm (142 liters/sec) at 1.8 gpm (6.8 liters/min) of coolant flow and the total cooling capacity was 9.0 MBtu/hr (2638 kilowatt). The fan coil units were connected to a set of remote temperature controllers. With the help of the temperature controller, a wide range of temperature options was available.

A mixture of 50% propylene glycol and 50% water mixture was used as coolant for the cooling circuit. A differential scanning calorimeter was used to obtain the desired properties of the mixture.

4. Indoor and outdoor conditions

For the experimental setup in the University of Kansas campus in Lawrence, Kansas, a 39°F (4°C) inside temperature was selected. Lawrence is situated at latitude of 38°57′36″N and a longitude of 95°15′12″W. Lawrence has a wide range of temperatures in different seasons. The average low temperature during winter is almost 20 °F(−7°C) in January, which reaches an average high above 90°F(32°C) in July [25]. Usually the first fall freeze occurs between mid-October and the second week of November and the last spring freeze occurs between the last week of March and the third week of April. The total amount of precipitation may be anywhere between 1 inch to 54 inches (27 to 1,400 mm) in a given typical year. Winter snowfall averages almost 18 inches (457 mm), but the median is less than 10 inches (250 mm). Lawrence experience maximum heat index temperature of 109 °F (43°C) and minimum wind chill temperature of 5°F to 10°F (−15°C to − 12 °C) . The maximum solar load value during summer is approximated 300 $\mathrm{Btu/ft^2/hr}$ (946 $\mathrm{W/m^2}$) and minimum solar load value during winter is approximated 163 $\mathrm{Btu/ft^2/hr}$ (514 $\mathrm{W/m^2}$).

5. Measurements

Temperatures and heat fluxes were measured at different locations. 'T' Type thermocouples were used to measure temperature. The grid network was designed in such a way to give average surface temperature for each panel. Indoor air temperatures were also measured. In addition to these, thermocouples were installed to measure coolant temperature into and out of the fan coil units in both the simulators. Heat flux meters were used to measure the heat fluxes across the walls. The size of the heat flux sensors was 2 in × 2 in (5.08 cm × 5.08 cm). The heat flux sensors were placed in such a way to give accurate values of the heat transfer rate across the panels. Except for the bottom panel, the heat flux sensors were placed in all panels. A data logger and laptop were used for on-site data collection and storage. Figure 15 shows the grid network used for temperature and heat flux measurement.

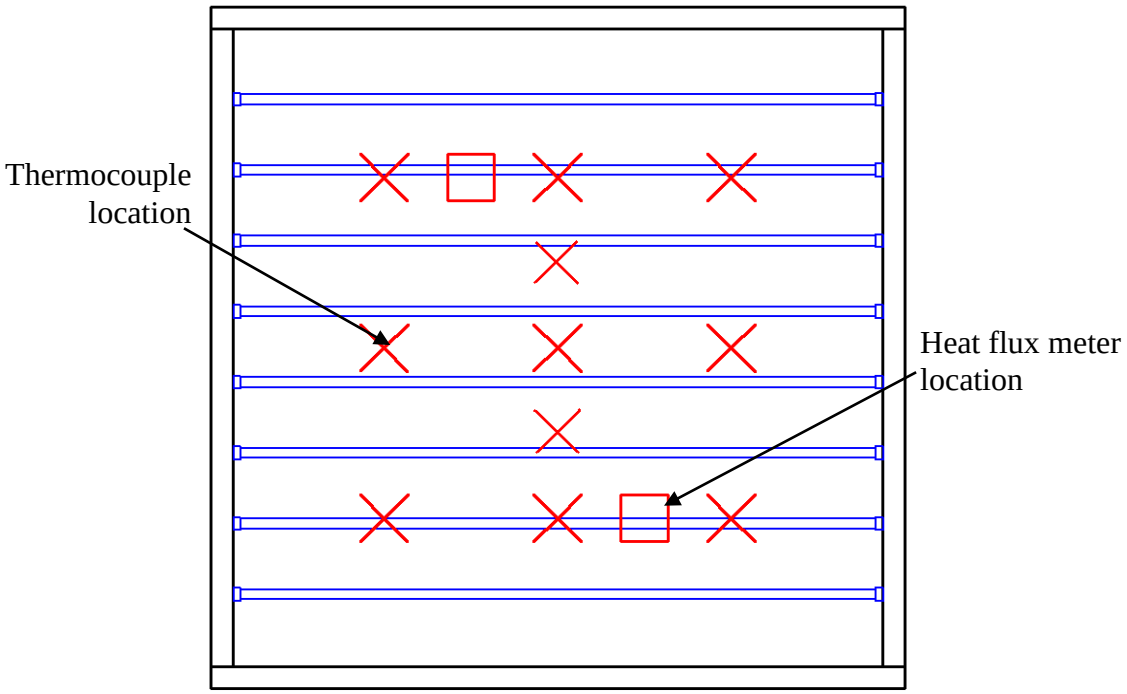

Figure 15: Thermocouple and heat flux meter (HFMs) locations [8]

Figures 16 and 17 show the thermocouple grid on the inside and outside of the simulators. Aluminum tape was used to adhere them to the walls.

Figure 16: Thermocouple grid on the outside surfaces of the simulator [8]

Figure 17: Thermocouple grid on the inside surfaces the simulator [8]

Table 2: Sensors and their accuracy [8]

Sensor	Range	Accuracy	Sensitivity
Heat flux meter	0 to 98287.8 Btu/ft^2/ hr (0 to 3.1×10^5 W/m^2)	2%	
Thermocouple T type	−0.4°F to 199.4°F (-18 °C to +93°C)	33°F (0.6°C)	
Pyranometer	−4°F to 104°C (-20 °C to 40°C)	±1%	8.82×10^{-6} volt/W.m^{-2}
Water flow meter	1.89 to 56.78 l/min (0.0667 cfm to 2.01 cfm)	±2%	4-20 mA
Thermostat	24°F to 219.99°F (-4.44°C to +104.44°C)	±33°F (±0.56°C)	4.8 ohms/°F
Atmospheric pressure*	28.2 in Hg to 30.7 in Hg (717.4 to 780.5 mm Hg)	0.05 in Hg (1.27 mm Hg)	
Rain fall Sensor*	unlimited	±4%	
Relative humidity*	0 to 100%	±3%	
Wind speed*	0 to 183 ft/s (0 to 55.9 m/s)	±1.48 ft/s (±0.45 m/s)	
Wind direction*	0 to 360°	±3%	
Outdoor temperature*	24°F to 140°F (-4.44°C to +60°C)	±33°F (±0.6°C)	

*Various components of the weather station.

The measurement of various parameters was one of the most crucial parts of the project. Preferences were given to the accuracy of the devices for different measurements. Table 2 gives detailed information about sensor, accuracy and sensitivity. Figures 18 and 19 show the remote thermostat and its controller. It was set to 39°F (4°C) and the differential was 33°F (0.5°C). Figures 18 and 19 show the thermostat probe inside the simulator and remote thermostat controller inside the equipment house.

Figure 18: Thermostat probe inside the simulator [8]

Figure 19: Remote thermostat controller inside the equipment house [8]

Figure 20 shows the heat flux meters.

Figure 20: Heat flux meters [8]

On the south, east and top walls, two heat flux meters were installed. One heat flux meter was used for each of the north and west walls. A weather station was set up in the experiment site. The weather station monitored air temperature, relative humidity, wind speed, wind direction and ambient pressure. An incident spectral pyranometer was also setup, which measured total solar spectral radiation data.

Figures 21 and 22 show the weather station and pyranometer.

Figure 21: Weather station with anemometer, rain fall gauge, and relative humidity sensor [8]

Figure 22: Pyranometer [8]

6. Data acquisition system

A data acquisition system was used to record and store the experimental data. The data logger had three 20-channels multiplexer. The type of connection used between the data logger and the laptop was RS-232 connection, which was controlled by software installed on the computer. A similar connection was made between the weather station and a computer. Data from the computer were downloaded to other workstations for post processing analysis. Figure 23 shows the data acquisition unit.

Figure 23: Data acquisition unit [8]

Figure 24 shows the laptop unit for the weather station.

Figure 24: Laptop unit for the weather station [8]

7. PCM selection

PCMs are categorized based on their melting point and latent heat values. Based on the inside air temperature of the containers, 39°F (4°C) and the average outdoor air temperature of the location, some PCMs were shortlisted. An in-house computer program that simulated PCMs in actual working condition was used to select the PCMs. Those with a solidification temperature above the inside temperature of the simulators were found suitable. A paraffin-based PCM (properties in Table 3) possessing the desired characteristics was selected.

Table: 3 PCM properties [38]

Property	Description
Melting point (approx.)	typical being 41°F (5°C)
Congealing point (PCM)	typical being 41°F (5°C)
Heat storage capacity, 28°F to55°F (-2°C to 13°C)	85 Btu/lb (198 kJ/kg)
Density solid, 5°F (−15°C)	7.3 lb/gal (0.88 kg/l)
Density liquid , 59°F/158°F (15°C/70°C)	6.4 lb/gal (0.77 kg/l)
Volume expansion	14%
Kinetic viscosity at 122°F (50°C)	0.03 in^2/s (18.92 mm^2/s)
Heat conductivity	0.35 Btu/hr − ft − f (0.2 W/mK)
Flash point (PCM)	251°F (122°C)
Corrosion	chemically inert with respect to most materials
Water hazard	water hazard class (WGK) 1

Chapter IV - Typical meteorological data

1. Introduction

A typical meteorological year (TMY) is a collation of weather data for a particular location, derived from a data bank much longer than a year in duration. It is designed in such a way that they present the range of weather variations for a particular location, but still provides typical weather information that is consistent with the long-term data. The typical meteorological year (TMY) data provide sufficient information for designers.

A TMY data cannot be used for weather forecast. On the other hand they provide typical weather information over a long period of time. TMY data sets are generally used by building designers and modelers. TMY data sets have natural periodic and seasonal variations and provide weather phenomena for a location from January 1 to December 31. [26].

TMY data sets consist of 12 typical months from January to December. These data sets contain actual time-series of meteorological measurements. Some hourly records may contain filled or interpolated data for periods, when original observations were missing. The TMY data sets and manuals were produced by the National Renewable Energy Laboratory's (NREL), and funded by the U.S. Department of Energy's Office of Solar Energy Conversion [29].

2. TMY2 data

The TMY2 data set contains weather data collected from 1961-1990. To identify each city in TMY2 data, a Weather Bureau Army Navy (WBAN) identification number was assigned to each station. TMY2 stations are classified as primary (P) or secondary (S) stations [29]. In total, there are 56 primary stations with measured solar radiation for a part (from 1 to 27 years) of the 30-year period [29]. The remaining 183 stations are classified as secondary stations with no solar

radiation measurements, and therefore, they used modeled solar radiation data that were derived from meteorological data such as cloud cover.

3. TMY3 data

The first TMY data set for the United States was introduced by Sandia National Laboratories in 1978 for 248 locations using long-term weather and solar data from the 1952–1975 SOLMET/ERSATZ database [26]. In 1994, NREL updated the TMY using data from the 30-year 1961–1990 National Solar Radiation Data Base (NSRDB) [27]. In 2007, NREL released a 15-year updated NSRDB for 1991–2005 [28]. The TMY3 data described here have more than 1,400 stations. The main objective of the TMY3 data was to maximize both the number of stations and the number of years from which to qualify the typical conditions of the locations.

TMY2 and TMY3 data sets have few differences, which gives utmost importance to solar radiation and meteorological elements. Both TMY2 and TMY3 data sets were created using procedures similar to those developed by Sandia National Laboratories [26].

The selection of the data used in the twelve months that form the typical meteorological year for each station was based on statistics, by considering five major elements like: global horizontal radiation, direct normal radiation, dry bulb temperature, dew point temperature, and wind speed. These elements were considered as the most important factors for solar energy conversion systems and building systems simulation.

4. TMY3 data format

The TMY3 format is entirely different from the previous TMY and TMY2 data sets. The TMY data set used positional formats, which optimized data storage space. These formats were difficult to read and difficult to import. The Comma Separated Value (CSV) format is a universal method which many software programs and software

packages have in built functions to read it. To facilitate this, the TMY3 data sets are provided in CSV format. The technical fields in TMY3 and TMY2 data sets are similar. The major differences between these two data sets are format and measurement units. For each station in the TMY3 data sets a United States Air Force (USAF) code is given. For example 999999TY.CSV, where 999999 refers the six digits USAF station identifier [30].

Chapter V: Estimation of solar loads on the various surfaces of the tractor trailer truck

1. Introduction to the solar model

In order to understand and justify, how PCMs respond to dynamic climatic conditions, simulation, observation, data collection and analysis information of moving truck trailers was necessary. Furthermore, an understanding of weather conditions in the Continental United States is needed to effectively select the most appropriate PCM. To achieve this goal, three important parameters, the solar loads, wind chill temperatures and interior surface temperatures were estimated for all the surfaces of a moving truck trailers using TMY weather data sets. In this research work, the solar load and wind chill temperature were estimated on all the walls (south, east, north, west, and top) of a truck trailer moving from one location to another location for every one hour and for four different seasons (fall, winter, summer and spring). The solar model was developed using Python, which is a script writing, high level programming language. The estimation of solar loads, wind chill temperatures and interior surface temperatures involved a combination of several parameters, including truck location and movement with respect to the sun and weather data for each location, where the truck was travelling. Figure 25 shows the flowchart used for the solar load calculations.

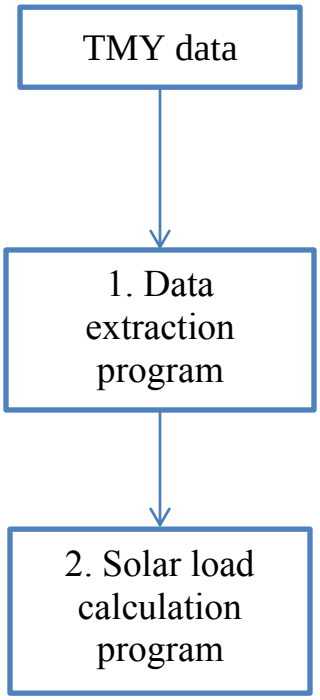

Figure 25: Flowchart of solar load calculation

2. Data extraction

The data extraction program was used to extract required fields from the TMY3 data files. TMY3 data contains many parameters like extraterrestrial horizontal radiation, global horizontal radiation, global horizontal illuminance, total sky cover, dry bulb temperature, dew point temperature, wind speed, wind direction, relative humidity, ceiling height, snow depth and many more data which were not required for calculating the solar loads and wind chill temperatures. Therefore the data extraction program extracted certain fields from the TMY3 data, and converted them into the required units, and saved them in separate weather data files, which were later used for the estimation of solar loads, wind chill temperatures and interior surface temperatures.

3. Solar load program

In the solar model, the solar load was calculated for tilted or vertical surfaces from available horizontal total insolation in the TMY3 files. The horizontal solar radiation was divided into beam and diffuse radiation. The method used to calculate the solar load was based on the model described by Reindl, Beckman and Duffie [31].

The next few paragraphs give basic definitions of the parameters used to calculate the solar loads.

Beam radiation: is the solar energy from the sun that reaches earth without scattering by the earth's atmosphere. Beam radiation is also referred to as direct solar radiation

Diffuse radiation: is the solar energy radiated from the sun whose direction gets scattered by the atmosphere. Diffuse radiation is also referred as sky radiation or solar sky radiation in some of the meteorological literature.

Total solar radiation: is the sum of the beam and diffuse radiations on a surface. The most common method of measuring solar radiation on a horizontal surface is using the total radiation. This radiation is also referred to as global radiation on the surface.

Irradiance and Insolation:

Solar irradiance is the amount of solar energy emitted by the sun at different wavelengths combining low-energy infrared photons $(1.1\ \text{eV})$ with high-energy ultraviolet photons $(3.5\ \text{eV})$ [32] and all the visible-light photons in between. This energy is measured from one square meter perpendicular plane outside the earth's atmosphere at a given distance from the sun. This irradiance on the outer surface of the earth's atmosphere is referred to as solar constant, G, which is approximately $433\ \text{Btu}/\text{ft}^2/\text{hr}\ (1367\ \text{W}/\text{m}^2)$ [32]. Figure 26 explains the sun-earth relationship.

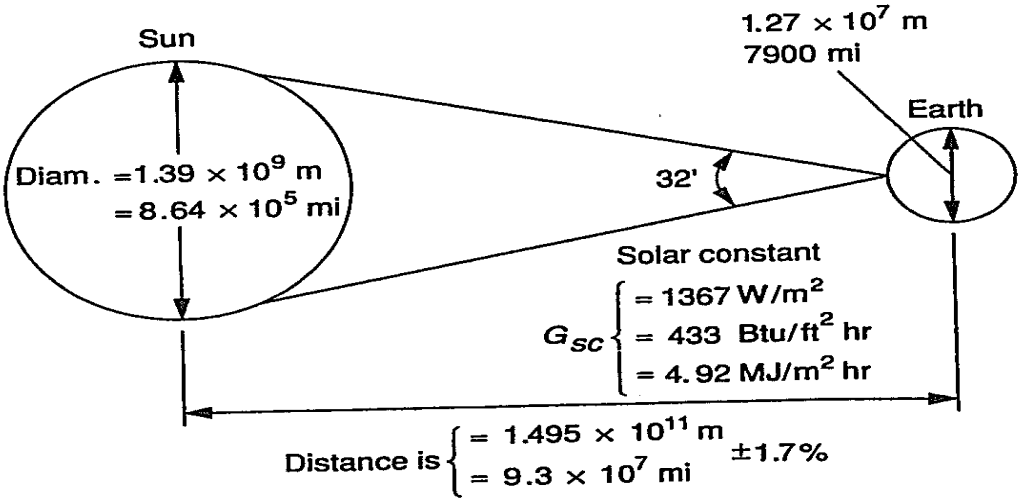

Figure 26: Sun-earth relationship [32]

As the altitude increases, insolation also increases. Figure 27 shows the spectrum of the solar energy impinging on a plane, directly facing the sun, outside the earth's atmosphere at the earth's mean distance from the sun. The area under the curve represents the total energy in the spectrum, G.

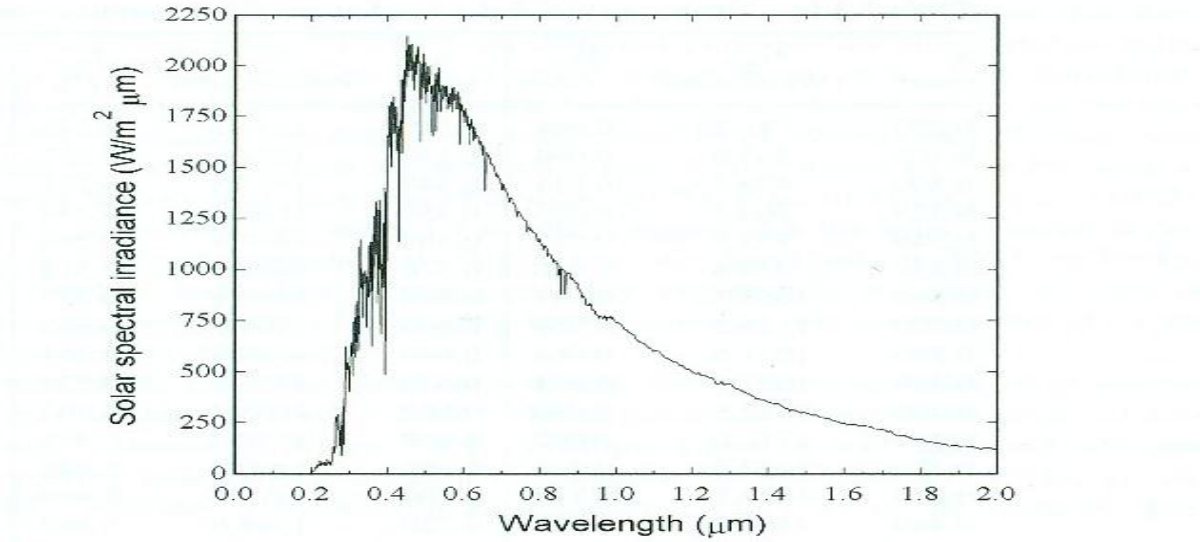

Figure 27: Standard spectral irradiance curve at the mean earth-sun distance [32]

The earth's orbit and rotation: The earth's rotation defines our day and night. The earth on average takes 24 hours to complete one rotation about its own axis relative to the sun in an elliptical orbit with the sun at one of the foci of the ellipse. Because of this, the insolation on the earth surface varies from maximum to minimum (i.e.). The maximum is at close to mid-day and comes to zero during the night. The orbital speed of the earth around the sun averages 18.64 miles/sec (30 km/s) [34].

Since the path of the earth around the sun is almost circular, the effect of the orbit on solar irradiance remains essentially constant throughout the year as the earth orbits the sun, but the solar irradiance varies as the season changes. The actual energy received by the earth at any distance from the sun is determined by the inverse square law. Thus a 3% change in distance gives rise to a 6% change in the irradiance.

The earth's tilt:

The earth rotational axis is tilted at an angle of 23.45 degrees from its plane of orbit. The earth axial tilt is the result of the gyroscopic effect of earth rotation, and it points towards the same direction throughout the year, such that the north pole of the earth point towards the North Star. The tilt of the earth as it orbits around the sun, in an elliptical path, determines the length of the day, intensity of the solar radiation or insolation. During the summer solstice, the northern hemisphere points towards the sun and the southern hemisphere will be away from the sun; during winter solstice, the northern hemisphere will have its shortest day. In spring (March) and autumn equinoxes (September), when earth is mid-way between the winter and summer solstices, the day and nights are of the same length. During the spring and autumn, the earth tilt is perpendicular to the direction of the sun from the earth; as a result the insolation will be the same on both hemispheres.

Latitude, $\emptyset$: Latitude of a location on the earth is the angular distance of the particular location north or south of the equator. Latitude is an angle and it is usually expressed in terms of degrees. The North Pole has latitude of 90° north and the South Pole has latitude of 90° south.

Slope, β: Slope is the angle between the plane of the surface and the horizontal; $0 \leq \beta \leq 180°$. (If slope $\beta > 90°$, then the surface has a component facing downward).

To understand the sun's path across the sky one needs to know the solar azimuth angle, elevation angle and hour or solar angle. Figure 28 gives a pictorial view of zenith angle, slope, surface azimuth angle and solar azimuth angle for a tilted surface and a plane view of solar azimuth angle. The following paragraphs explain each step of the solar load calculation.

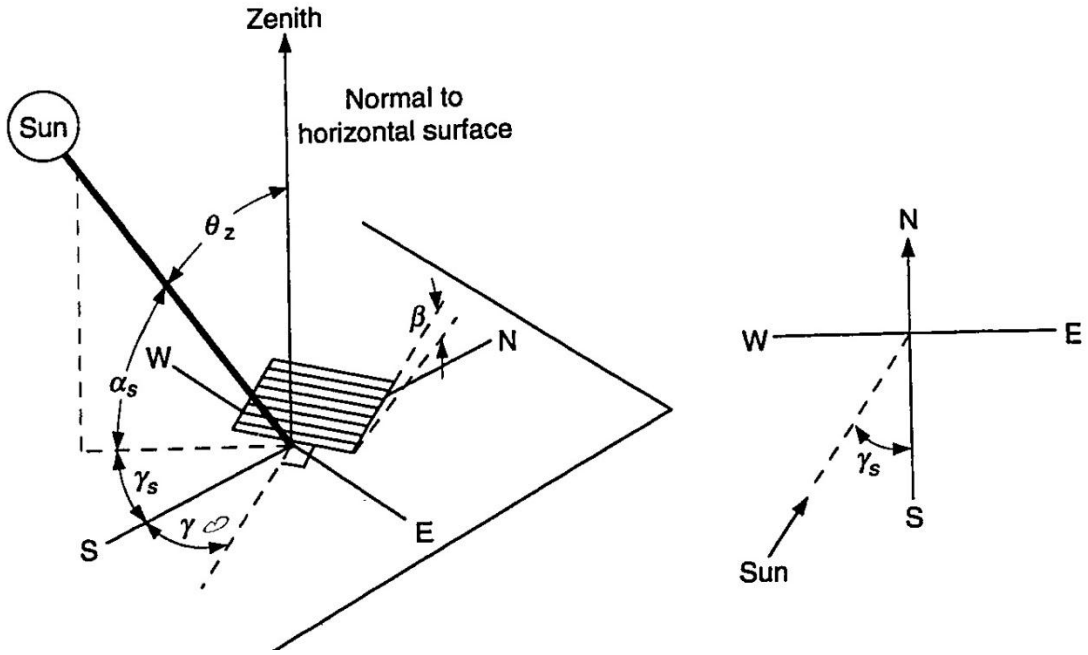

Figure 28: Pictorial representation of zenith angle, slope and solar azimuth angles [32]

4. **Solar azimuth angle, γ_s:** Solar azimuth angle is the angular displacement from south of the projection of the beam radiation on the horizontal plane or it is the angle from north in a clockwise direction. It can be calculated, using the following equations, however care should be exercised because the inverse sine, i.e. x= $\sin^{-1}(y)$, has more than one solution and only one of which will be correct.

The following equations can be used to find the solar azimuth angle, however the azimuth angle will be always positive (i.e.) less than 180 degrees with negative hour angle or solar angle. On the other hand the solar azimuth angle will be greater than 180 degrees with positive hour angle or solar angle.

$$\sin \gamma_s = \frac{-\sin \omega * \cos \delta}{\cos \alpha_s} \qquad \text{Eq. 1}$$

$$\cos \gamma_s = \frac{\cos \omega * \cos \delta * \sin \emptyset - \sin \delta}{\cos \alpha_s} \qquad \text{Eq. 2}$$

$$\cos \gamma_s = \frac{\sin \alpha_s * \sin \emptyset - \sin \delta}{\cos \alpha_s * \cos \emptyset} \qquad \text{Eq. 3}$$

Where α_s is the solar elevation angle, ω, the hour angle of the present time, δ is the sun declination, and $\emptyset$ is the local latitude. The solar azimuth angle is calculated as

5. **Equation of Time (ET):** The equation of time (ET) (in minutes) is an empirical equation that corrects for the eccentricity of the earth's orbit and the earth's axial tilt.

$$\text{ET} = 9.87 * \sin(2\text{B}) - 7.53 * \cos(\text{B}) - 1.5 * \sin(\text{B}) \qquad \text{Eq. 4}$$

$$\text{where, } \text{B} = \frac{360}{365}(\text{d} - 81)$$

and d is the day of the year (e.g. d=15 on Jan 15 and d=46 on Feb 15). The time correction ET is plotted in Figure 29.

Time correction factor (TC): To account for the variation in the local solar time due to the longitude variations within the time zone, a correction factor has to be implemented along with Equation of Time.

$$\mathrm{TC} = 4(\mathrm{Longitude} - \mathrm{LSTM}) + \mathrm{ET} \qquad \text{Eq. } 5$$

$$\mathrm{LST} = \mathrm{LT} + \frac{\mathrm{TC}}{60} \qquad \text{Eq. } 6$$

Where LST is local solar time and LT is local time.

The factor of 4 minutes comes from the fact that the earth rotates 1° every 4 minutes.

The Local Standard Time Meridian (LSTM) is a reference meridian used for a particular time zone and is similar to the prime meridian, which is used for Greenwich Mean Time.

Once the time correction factor has been calculated, the true solar time can be calculated,

$$\mathrm{TST} = \mathrm{LST} + \mathrm{TC} \qquad \text{Eq. } 7$$

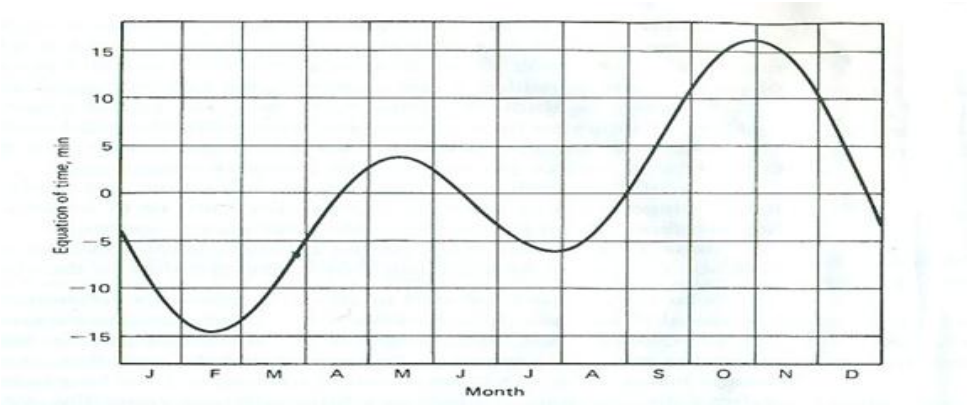

Figure 29: Equation of Time (ET) in minutes as a function of time of year [32]

6. **Hour angle or solar angle, ω:** The hour angle or solar angle is measured in the plane of the apparent orbit of the sun as it moves across the sky. Since the earth rotates 15° per hour and moves through 360 degrees over the entire day, each hour away from solar noon period corresponds to an angular motion of the sun in the sky of 15°. In the

morning, the hour angle is negative, in the afternoon the hour angle is positive. Typically, the hour angle is said to be zero at solar noon, when the sun is at the zenith or highest in the sky. The hour angle or solar angle is used to convert the local solar time (LST) into the number of degrees which the sun moves across the sky.

$$\omega = 15°(12 - \mathrm{TST}) \qquad \text{Eq. } 8$$

7. **Sun declination angle, δ:** Sun declination angle is the angle between the rays of the sun and the plane of the earth's equator. The sun declination angle varies as a result of the earth's tilt about its axis of rotation. If the earth were not tilted, the declination angle would be zero. Since the earth is tilted by $23.45°$, the declination angle varies by $+23.45°$ or $-23.45°$. The declination angle can be found by

$$\delta = \sin^{-1}\left\{\sin(23.45°)\sin\left[\frac{360}{365}(\mathrm{d} - 81)\right]\right\} \qquad \text{Eq. } 9$$

However the declination angle can also be calculated from the following equations,

$$\delta = -23.44° * \cos\left[\frac{360°}{365} * (\mathrm{d} + 10)\right] \qquad \text{Eq. } 10$$

$$\delta = 23.44° * \sin\left[\frac{360°}{365} * (\mathrm{d} + 284)\right] \qquad \text{Eq. } 11$$

Where d is the number of days elapsed since January 1. Figure 30 shows the position of earth during the summer solstice and the respective declination angle.

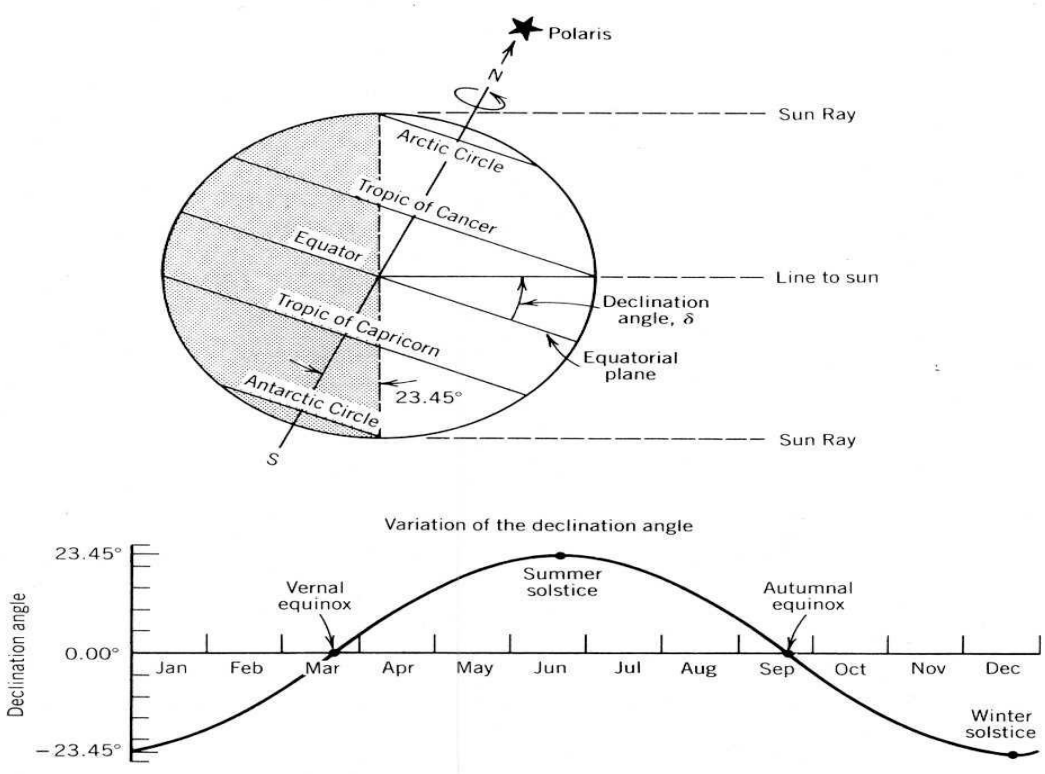

Figure 30: Declination angles and position of the earth during the summer solstice [35]

8. Extraterrestrial radiation: Solar radiation incident outside the earth's atmosphere is called extraterrestrial radiation. On average the extraterrestrial irradiance is 433 Btu/ ft^2/hr (1367 W/m^2). This value varies by $\pm 3\%$ as the earth orbits the Sun [32]. The earth's closest approach to the sun occurs around January 4th and it is farthest from the sun around July 5th. The variation of the earth-sun distance, however, does lead to variation of extraterrestrial radiation flux in the range of plus or minus 3.3% [32]. The extraterrestrial radiation incident on the plane normal to the radiation on the nth day of the year can be calculated by using the following equations.

$$I_O = I_{SC}\left(1 + 0.033 * \cos\left(\frac{360d}{365}\right)\right) \qquad \text{Eq. 12}$$

$$I_O = I_{SC}(1.000110 + 0.034221\ \cos B + 0.001280\ \sin B + 0.000719\ \cos 2B + 0.000077\ \sin 2B) \quad \text{Eq. 13}$$

Where,

$I_O -$ is the extratrestrial radiation on the plane normal to the radiation on the dth day of the year and B is given by

$$B = (d - 1)\frac{360}{365}$$

$I_{SC} -$ Solar constant, 433 $Btu/ft^2/hr$ $(1367\ W/m^2)$

9. **The zenith angle, θ_z:** is the angular distance between the line towards the center of the sun and the local zenith, relative to the point for which the zenith is defined. Figure 31 shows the zenith angle.

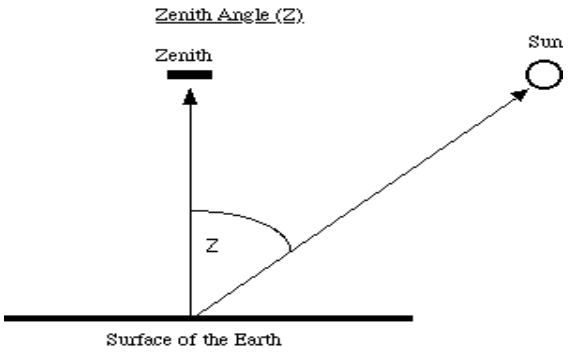

Figure 31: Zenith angle [33]

In equation form: Zenith angle

$$= \cos^{-1}\{\cos(\delta) * \cos(LAT) * \cos(\omega) + \sin(\delta) * \sin(LAT)\} \quad \text{Eq. 14}$$

10. **Solar altitude angle or elevation angle α_s:** Solar altitude angle is the angle between the horizon and the line towards the center of the sun. The solar altitude angle is 0 degrees at sunrise/sunset and, 90 degrees at the zenith or overhead.

$$\text{Solar altitude angle} = 90 - ZAD \quad \text{Eq. 15}$$

11. Calculation of K_T beam and diffuse components of hourly radiation:

In solar energy systems, one important factor is the hourly radiation incident on a surface. But for the surface slope and orientation under consideration, hourly solar radiation is non-existent. From TMY2 and TMY3 data sets, the information for hourly global radiation on a horizontal is available.

When only global horizontal radiations were measured using TMY2 and TMY3 data sets, then there are two problems. The first problem in determining the fractions of the global horizontal radiation, that are both diffuse and beam. The second problem is projecting the beam radiation onto a tilted surface of any orientation. Liu and Jordan [31] proposed a relationship between daily diffuse and daily total radiation on a horizontal surface. Even though their original correlation was developed for daily values, later research allowed for calculating the hourly fractions as a function of the hourly clearness index, K_T (ratio of hourly global horizontal to hourly extraterrestrial radiation). Many authors had developed diffuse fraction correlations specifically for hourly intervals like Orgill [31] and Hollands and Erbs [31] which correlate diffuse fraction with the hourly clearness index. Sauter and Klein [31] used a clearness index K_C, where a clear sky radiation,$I_{C,}$ was used instead of extraterrestrial radiation in the definition of K_T. The major drawback of Liu and Jordan model was the high standard error in estimating the hourly diffuse fraction. In this work, the model developed by Reindl, Beckman and Duffie [31] is used, which reduced the standard error of Liu and Jordan type models.

The graphs of Figures 32 and 33 show the measured diffuse fraction correlation value of Erbs [31], Liu and Jordan [31], Ktcorr, Orgill and Hollands [31]. The diffuse fraction correlations are given by the following equations.

$$\frac{I_d}{I} = 1.0 - 0.09K_T, \text{for } K_T \leq 0.22 \quad \text{Eq. 16}$$

$$\frac{I_d}{I} = 0.9511 - 0.1604K_T + 4.388K_T^2 - 16.638K_T^3 + 12.336K_T^4, \text{ for } 0.22 < K_T \leq 0.80 \quad \text{Eq.17}$$

$$\frac{I_d}{I} = 0.165, \text{for } K_T > 0.8 \quad \text{Eq. 18}$$

Therefore the horizontal beam and diffuse radiation can be calculated by,

$$\text{Horizontal diffuse radiation , DIFH} = \left(\frac{I_d}{I}\right) * \text{QSOLH} \quad \text{Eq. 19}$$

$$\text{Horizontal beam radiation , BEAMH} = \left(1 - \frac{I_d}{I}\right) * \text{QSOLH} \quad \text{Eq.20}$$

$$\text{Total horizontal solar radiation , I} = \text{BEAMH} + \text{DIFH} \quad \text{Eq. 21}$$

Where, QSOLH is global horizontal radiation.

Figure 32 and 33 also explain the measured diffuse fraction vs clearness index for Cape Canaveral, FL and diffuse fraction correlations.

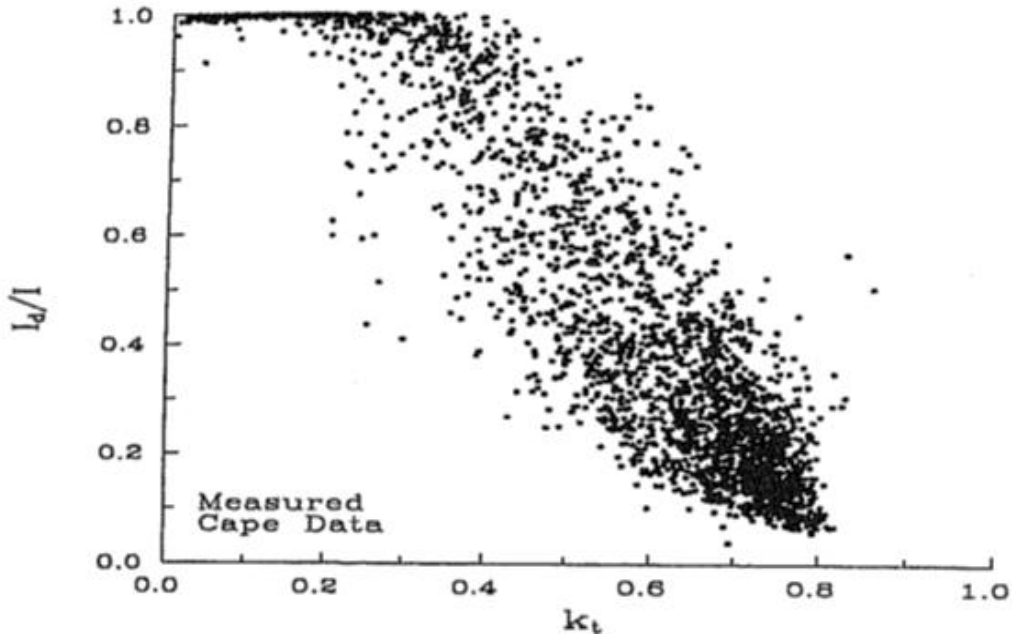

Figure 32: Measured diffuse fraction vs. clearness index for Cape Canaveral, FL [31]

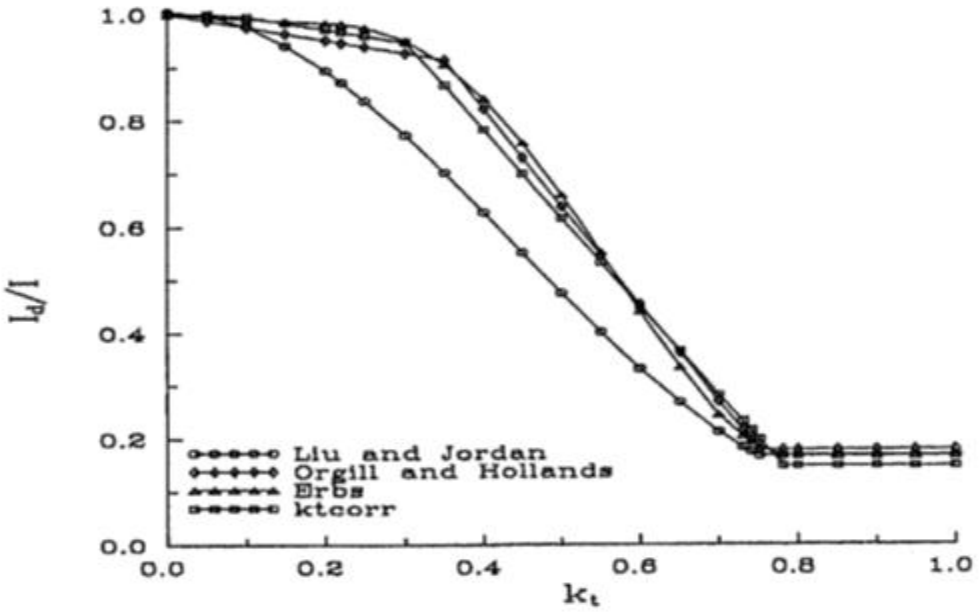

Figure 33: Diffuse fraction correlations [31]

12. Ratio of beam radiation on a tilted surface to that on a horizontal surface: From TMY2 and TMY3 data sets, the hourly solar radiation on a horizontal surface can be obtained, but there is a need to find hourly solar radiation on a tilted surface. Figure 34 shows the angle of incidence of beam radiation on a horizontal and tilted surface. The geometric factor R_b is the ratio of beam radiation on a tilted surface to beam radiation on a horizontal surface at any time and can be calculated by using the following equation.

$$R_b = \frac{G_{b,T}}{G_b} = \frac{G_{b,n}\cos\theta}{G_{b,n}\cos\theta_Z} = \frac{\cos\theta}{\cos\theta_Z} \qquad \text{Eq. 22}$$

$$\text{Where } \cos\theta = \cos(\emptyset - \beta) * \cos\delta * \cos\omega + \sin(\emptyset - \beta) * \sin\delta$$

$$\cos\theta_Z = \cos\emptyset * \cos\delta * \cos\omega + \sin\emptyset * \sin\delta$$

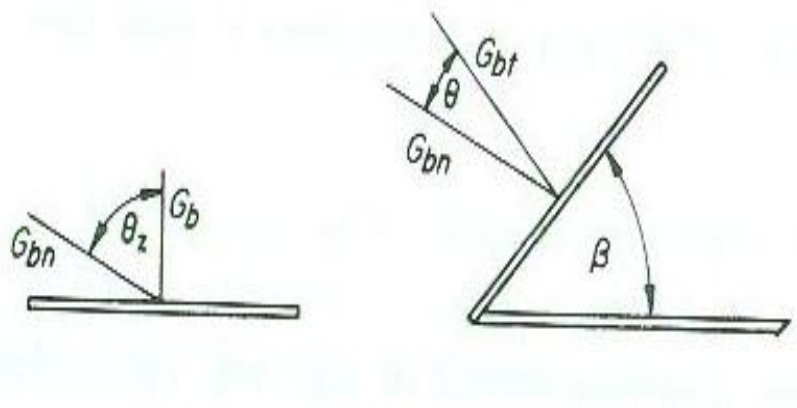

Figure 34: Beam radiation on a tilted and a horizontal surface [32]

13. Total solar radiation on a tilted surface: In 1942 Hottel and Woertz [32] suggested that the combination of diffuse and ground-reflected radiation is isotropic (uniformity in all orientations). This suggestion leads to the assumption that the sum of the diffuse from the sky and the ground-reflected radiation on a tilted surface is the same regardless of orientation. The total radiation on a tilted surface for an hour is the sum of the beam contribution calculated as $\mathrm{BEAMH} * \mathrm{R_b}$ and the diffuse radiation on a horizontal surface, DIFH.

$$\text{The total solar radiation on a tilted surface for an hour, IT} = \mathrm{BEAMH} * \mathrm{R_b} + \mathrm{DIFH} \qquad \text{Eq. 23}$$

However an improvised model was created by Liu and Jordan [32] called as the isotropic diffuse model. The radiation on a tilted surface should include all the three components such as beam, isotropic diffuse, and solar radiation diffusely reflected from the ground, where ρ_g is the diffuse reflectance of the surrounding. The total solar radiation on the tilted surface for an hour can be calculated by using the following equation.

$$\text{The total solar radiation on a tilted surface for an hour, IT} = \mathrm{BEAMH} * \mathrm{R_b} + \mathrm{DIFH} * \left(\frac{1+\cos\beta}{2}\right) + \mathrm{I}\rho_g * \left(\frac{1-\cos\beta}{2}\right) \qquad \text{Eq. 24}$$

14. Wind chill index: The national Weather Service in November 2001 [36] came up with a new wind chill index, used by the U.S. and Canadian weather services. The new wind chill index was determined under various wind speeds and temperatures. This wind chill index model used standard engineering correlations of wind speed and heat transfer rate. Heat transfer rate was calculated for a surface, facing the wind and walking into at

it 3.1 mph (5.0 kmh) [39]. The wind chill index can be calculated by using the following equation,

$$T_{wc} = 35.74 + 0.6215T_a - 35.75V^{+0.16} + 0.4275T_aV^{+0.16} \qquad \text{Eq. 25}$$

Where T_{wc} and T_a are measured in °F (℃) , and V in mph (kph).

This wind chill temperature is only for temperatures at or below 50°F (10℃) and for wind speeds above 3.0 mph (5.0 kmh) [36]. As the air temperature falls, the chilling effect of any wind increases. Figure 35 gives detailed information about wind chill temperatures for different air temperatures and wind speeds.

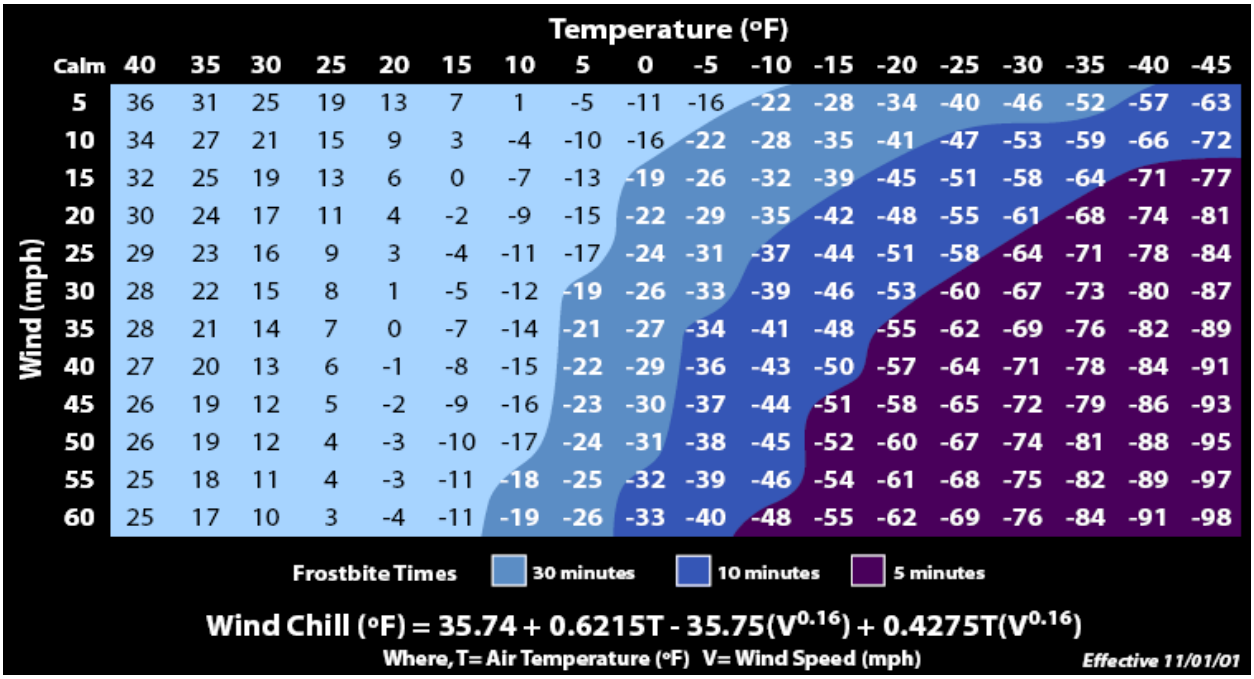

Figure 35: Wind chill temperatures for given air temperatures and wind speeds [36]

15. Quasi steady-state heat transfer across the walls of refrigerated tractor trailers:

The quasi steady state heat transfer (heat balance) across the walls of refrigerated tractor trailers involves four heat transfer flows: conduction into the walls of the truck, convection, solar absorption, and grey-body irradiation to the surroundings.

i. the heat flow contribution due to conduction is given by,

$$\frac{(T_{s,o} - T_{s,i})}{R} \qquad \text{Eq. 26}$$

Where,

$T_{s,o}$ – outside surface temperature of the truck

$T_{s,i}$ – inside surface temperature of the truck

R – polyurethane foam insulation

ii. the convection heat flow is given by,

$$h_{conv}(T_{s,o} - T_{ambient}) \qquad \text{Eq. 27}$$

$T_{s,o}$ – outside surface temperature of the truck

$T_{ambient}$ = ambient temperature

$$h_{conv} = h_{forced} + h_{free} \qquad \text{Eq. 28}$$

h_{conv} – heat convections due to both free and forced convections.

h_{forced} – forced heat convection.

h_{free} – free heat convection.

$$h_{forced} = 0.54\,(\frac{V^4}{L})^{\frac{1}{4}} \qquad \text{Eq. 29}$$

L- length of the surface in the direction of the flow.

V – velocity of the flow.

$$h_{free} = 0.19(\Delta T * \sin\beta)^{\frac{1}{3}} \qquad \text{Eq. 30}$$

$\Delta T -$ difference in temperature between the outside surface and the air

$\beta -$ is the angle of tilt (0° for horizontal and 90° for vertical)

iii. the radiation absorbed from the incoming sunlight, whose equation is given by

$$\alpha_{solar} * q_{sol} \qquad \text{Eq. 31}$$

$\alpha_{solar} -$ solar absorptivity of the surface, assumed as 0.65

$q_{sol} -$ incident solar radiation on the outside surface of the truck

iv. the emission of radiation from the "warm" truck walls to the night sky. This heat flow can be estimated as:

$$\sigma\epsilon_{surface}\left(T_{s,o}^4 - T_{sky}^4\right) \qquad \text{Eq. 32}$$

$\sigma -$ Stefan $-$ Boltzman constant $= 0.1714 * 10^{-8}$ Btu $hr^{-1}ft^{-2}$ R^{-4} (5.67×10^{-8} W m^{-2} K^{-4})

$T_{sky} -$ sky temperature,

$T_{s,o} -$ outside surface temperature of the truck

$\epsilon_{surface} -$ emissivity of the surface, assumed as 0.85

The sky temperature can be estimated based on an algorithm presented by Walton [41] using the following series of equations:

$$T_{sky} = \epsilon_s^{1/4} * T_{ambient} \qquad \text{Eq. 33}$$

$$\epsilon_s = 0.787 + 0.764 * \ln\left(\frac{T_{dew}}{273}\right) * F_{cloud} \qquad \text{Eq. 34}$$

$$F_{cloud} = 1.0 + 0.024N - 0.0035N^2 + 0.00028N^3 \qquad \text{Eq. 35}$$

$\epsilon_s -$ sky emissivity

F_{cloud} – cloud cover factor

T_{dew} – dew point temperature

N is the "tenths cloud cover", taking values between 0.0 and 1.0.

Therefore, the energy balance equation is given by,

$$\text{Energy}_{in} = \text{Energy}_{out} \qquad \text{Eq. 36}$$

$$\alpha_s q_{sol} = \sigma \varepsilon_{surface}\left(T_{s,o}^4 - T_{sky}^4\right) + h_{conv}\left(T_{s,o} - T_{ambient}\right) + \frac{(T_{s,o} - T_{s,i})}{R} \qquad \text{Eq. 37}$$

Chapter VI: Routes – across the Continental United States

1. Introduction

To find the solar loads, wind chill temperatures, and interior surface temperatures on various surfaces of the truck, eight different routes across the Continental United States were selected. The main reasons that influenced the choice of routes were mainly: 1) the need to cover a wide range of distance across the United States, 2) the need to cover different directions such as from north to south, east to west, south to north, and west to east and 3) the need to span different weather conditions during all the four different seasons (fall, spring, summer and winter). The routes that were selected were:

- Atlantic, NJ - Portland, ME
- Brownsville, TX - Baton Rouge, LA
- Chicago, IL - Pittsburgh, PA
- Columbus, GA - Bristol, TN
- Minot, ND - Sioux City, IA
- Rock Springs, WY - Omaha, NE
- Sacramento, CA - San Diego, CA
- Topeka, KS - Fort Worth, TX.

There were also other motivations behind choosing some of the above routes. For example Sacramento, CA to San Diego, CA route is one among the eight routes because a) nearly 90 percent of food items like vegetables and fruits consumed in the United States are transported from California State, b) during summers, California State faces very hot and humid climate

resulting in high solar energy falling on the surface of the truck. The route between Minot, ND to Sioux City, IA route was selected because of its extreme weathers, i.e. cold weather even during summers and wind chill temperature less than 0°F (℃).

In the following sections, a running example of the method adopted to obtain route specific weather data is detailed.

2. Minot, ND to Sioux City, IA

For Minot, ND to Sioux City, IA, (USAF code is 725744), the truck started at Minot by 7 AM and reached Underwood by 8 AM. The route followed by the truck to reach Underwood was US-83 S and the weather data of Minot was used for Underwood, as Underwood is close to Minot. After this, the truck went through the following locations: Bismarck, Linton, Selby, Pierre, Ree Heights, Huron, Mitchell, Sioux Falls and Sioux City. In Table 4 the route taken by the truck is mentioned with the locations, route, and distances between the locations and the USAF code for each location. Figure 36 shows the Minot, ND to Sioux City, IA route.

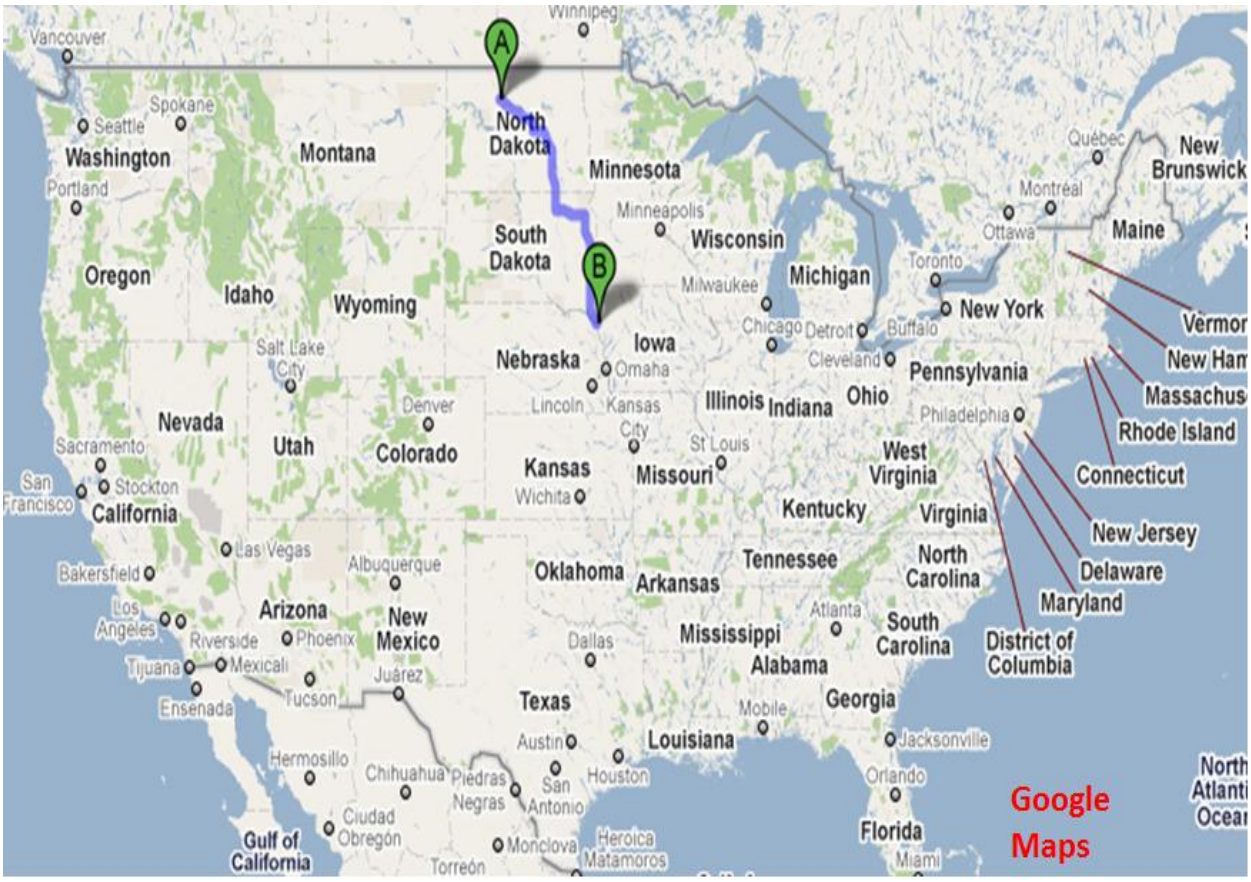

Figure 36: A route from Minot, ND to Sioux City, IA [37]

Table 4: Minot, ND to Sioux City, IA route with distance between locations, starting time and United States Air Force (USAF) code.

Place	Route	Distance, miles (km)	Arrival time	TMY3 data	USAF code
Minot, ND			7 AM		727675
Underwood, ND	US-83 S	57 (91)	8 AM	Minot	727675
Bismarck, ND	US-83 S	59 (94)	9 AM		727640
Linton, ND	US-83 S and I-94 E	66 (106)	10 AM	Bismarck	727640
Selby, SD	US-83 S	57 (91)	11 AM	Pierre	726686
Pierre, SD	US-83 S	88 (141)	12 PM		726686
Ree Heights, SD	US-14 E	61 (98)	1 PM	Huron	726540
Huron, SD	US- 14 E	60 (97)	2 PM		726540
Mitchell, SD	S Dakota 37 S	63 (101)	3 PM		726545
Sioux Falls, IA	S Dakota 42 E	71 (114)	4 PM		726510
Sioux City, IA	I-29 S	82 (132)	5 PM	Sioux Falls	726510

3. Sacramento, CA to San Diego, CA

. It was assumed that the truck started at 9 AM from Sacramento. The respective weather information for Sacramento can be obtained from TMY3 data and the United States Air Force code (USAF) 724839. The truck drove along I-80 W and CA-113 S to reach Oakley by 10 AM. As there is no weather information for Oakley, the weather data of San Francisco was taken, which is close to Oakley, when compared to Sacramento. Next, the truck took CA-4 W and I-80 W to reach San Francisco by 11 AM. After, this the truck went to the following locations: Tracey, Merced, Fresno, Tipton, Bakersfield, California City, Boron, Dagget, Lytle Creek, Los Angeles, Laguna Niguel and San Diego. For some of these locations, there were no TMY3 data. So, weather data from nearby locations were selected based on the distance between them. Figure 37 shows the Sacramento, CA to San Diego, CA route. Table 5, the route followed by the truck is mentioned with the locations, route, and distance between the locations and the USAF code for each location. The procedure mentioned above was used in all the remaining six routes too.

Figure 37: A route from Sacramento, CA to San Diego, CA [37]

Table 5: Sacramento, CA to San Diego, CA route with distance between locations, starting time and United States Air Force (USAF) code.

Place	Route	Distance, miles (km)	Arrival time	TMY3 data	USAF code
Sacramento			9 AM		724839
Oakley	I-80 W and CA-113 S	64 (103)	10 AM	San Francisco	724940
San Francisco	CA-4 W and I-80 W	58 (93)	11 AM		724940
Tracy	I-580 E	63 (101)	12 PM	San Francisco	724940
Merced	CA-33 S and CA-99 S	68 (109)	1 PM		724815
Fresno	CA-99 S	58 (93)	2 PM		723890
Tipton	CA-43 S and CA-99 S	66 (107)	3 PM	Bakersfield	723840
Bakersfield	CA-99 S	60 (98)	4 PM		723840
California City	CA-58 E/Barstow-Bakersfield Hwy/Blue Star Memorial Hwy	69 (111)	5 PM	Bakersfield	723840
Boron	US-395 S	72 (116)	6 PM	Dagget	723815
Dagget	CA-58 E/Barstow-Bakersfield Hwy/Blue Star Memorial Hwy	60 (97)	7 PM		723815
Lytle Creek	I-15 S	78 (126)	8 PM	Los Angeles	722950
Los Angeles	CA-60 W	65 (104)	9 PM		722950
Laguna Niguel	I-405 S and CA-73 S	60 (97)	10 PM	Los Angeles	722950
San Diego	I-5 S	70 (112)	11 PM		722900

Chapter VII: Result and discussions

The solar loads, wind chill temperatures and interior surface temperatures on the surface of the moving tractor trailers outfitted with phase change materials were calculated using a Python. To report the obtained results on solar load, wind chill and interior surface temperature calculation, two of the eight routes i.e., 1) Minot, ND to Sioux City, IA and 2) Sacramento, CA to San Diego, CA are selected. The results are presented for a sampled day from each of the four different seasons (fall, spring, summer and winter). The factors that influenced solar loads were mainly 1). Elevation of the location, 2). Opaque (the amount of sky completely hidden by clouds) and total sky cover (the amount of sky covered but not concealed). 3). The season of the year and the time of day. The following results show the behavior of solar load on each of the four seasons. Furthermore, they provide ample evidence to the effect of the above parameters on the recorded solar load.

1. **Solar loads – Minot, ND to Sioux City, IA:** Graphs presented in Figures 38 to 45 depict the solar loads for both horizontal and vertical surfaces of the truck for the Minot, ND to Sioux City, IA route. The graphs clearly show the variation in solar load for all the surfaces of the truck for the different seasons.

    a. **Fall season:** From Figures 38 and 39 it can be observed that the solar load on the top surface of the truck was almost zero at Minot until 8 AM, due to complete cloud cover. The top surface was exposed to solar load from 9 AM and reached a maximum value of $226\ \mathrm{Btu/ft^2/hr}$ $(712\ \mathrm{W/m^2})$ at Pierre by 12 PM. The reason for high solar load recorded at Pierre was due to zero sky cover (10 – represents sky domed entirely by clouds and 0 – represents clear

sky), even though Pierre is 528 meters (1732 ft) above sea level. On the other hand, the solar load on the north surface of the truck was almost negligible throughout the travel. It can be observed from Figure 39, that there was a sudden increase in solar load for the east surface of the truck from Underwood, ND (9 AM) to Bismarck, ND (10 AM). This was mainly due to difference in total and opaque sky cover between two stations. The south and east surface of the truck experienced a maximum solar load of $228\ \mathrm{Btu/ft^2/hr}$ ($719\ \mathrm{W/m^2}$) at Pierre by 12 PM and $223\ \mathrm{Btu/ft^2/hr}$ ($703\ \mathrm{W/m^2}$) at Selby by 11 PM, with zero sky cover, in spite of being at 528 meters (1732 ft) above sea level. The solar load on the east surface of the truck approached zero after 1 PM. The west surface of the truck received solar load only after 12 PM, and it reached a maximum value of $217\ \mathrm{Btu/ft^2/hr}$ ($684\ \mathrm{W/m^2}$) at Sioux Falls, SD by 4 PM, with zero sky cover. Figures 38 and 39 show the solar load on the horizontal and vertical surfaces of the truck during a day in fall season (Minot, ND to Sioux City, IA).

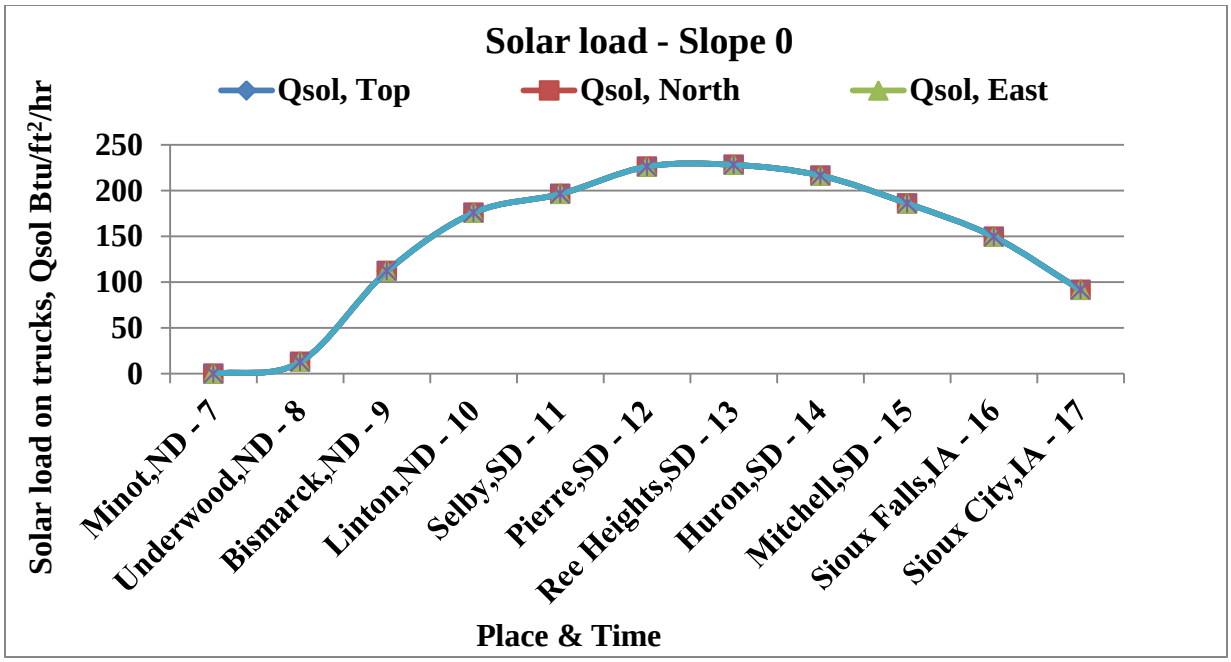

Figure 38: Solar load on the horizontal surface of the truck during a day in fall season (Minot, ND to Sioux City, IA)

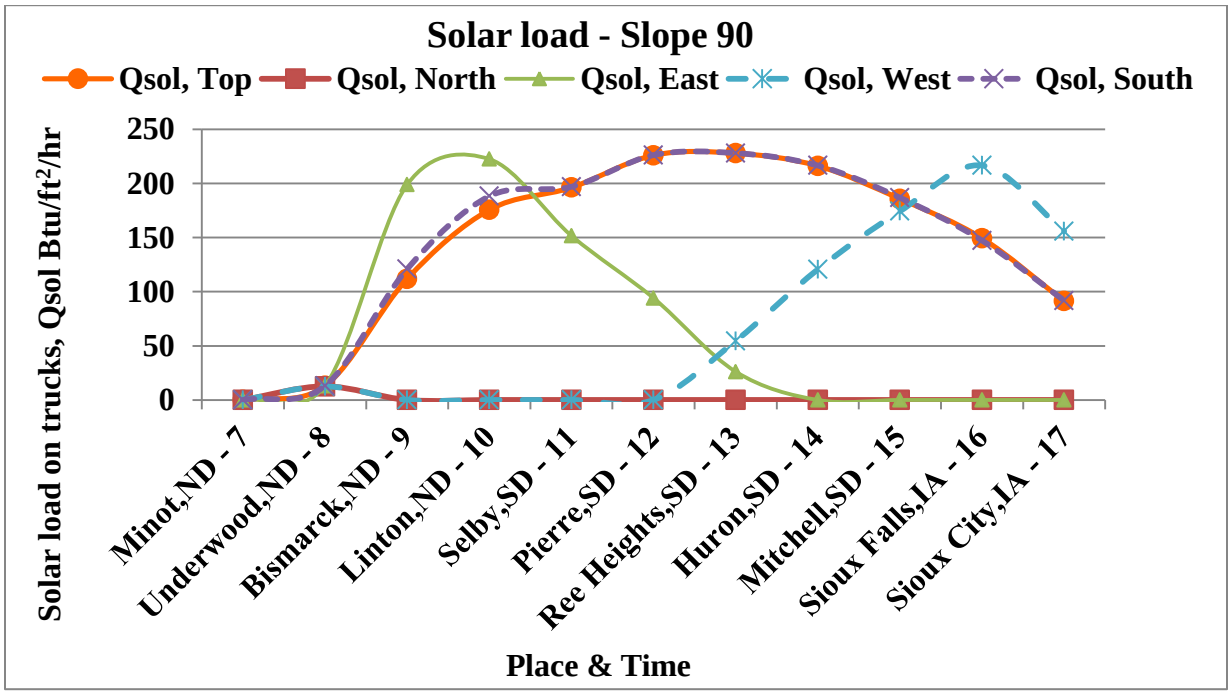

Figure 39: Solar load on the vertical surface of the truck during a day in fall season (Minot, ND to Sioux City, IA)

b. Spring season: Figures 40 and 41 summarize the solar load on horizontal and vertical surfaces of the truck for spring season. The solar load on the top surface of the truck reached a maximum value of $240\ \mathrm{Btu/ft^2/hr}$ ($757\ \mathrm{W/m^2}$) at Ree Heights by 1 PM, whose total and opaque sky cover was 2 and elevation of 390 meters (1279 ft) which is lowest among the intermediate stations between Minot, ND to Sioux City, IA. This resulted in relatively high solar load on the top surface of the truck. The solar load on the north surface of the truck was exposed to a maximum solar load of $79\ \mathrm{Btu/ft^2/hr}$ ($249\ \mathrm{W/m^2}$). This value was relatively high, when compared to the north surface of the truck during fall season. It's noticeable that there were minor fluctuations in the received solar load like in Figure 41, blue curve shows the variation in solar load of west surface of the truck between Ree Heights, SD (3 PM) to Sioux City, IA (5 PM), in spite of having same total sky cover, opaque sky cover and elevation. Here the variations were possibly due to other parameters like atmospheric effects, absorption and scattering and variations in the atmosphere, and pollutions (global warming). The south surface of the truck experienced a maximum solar load of $239\ \mathrm{Btu/ft^2/hr}$ ($753\ \mathrm{W/m^2}$) at Ree Heights by 1 PM, whose total sky cover was 9 and opaque sky cover was 3. The east surface of the truck experienced a maximum solar load of $148\ \mathrm{Btu/ft^2/hr}$ ($466\ \mathrm{W/m^2}$). Figures 40 and 41 show the solar load on the horizontal and vertical surfaces of the truck during a day in spring season (Minot, ND to Sioux City, IA).

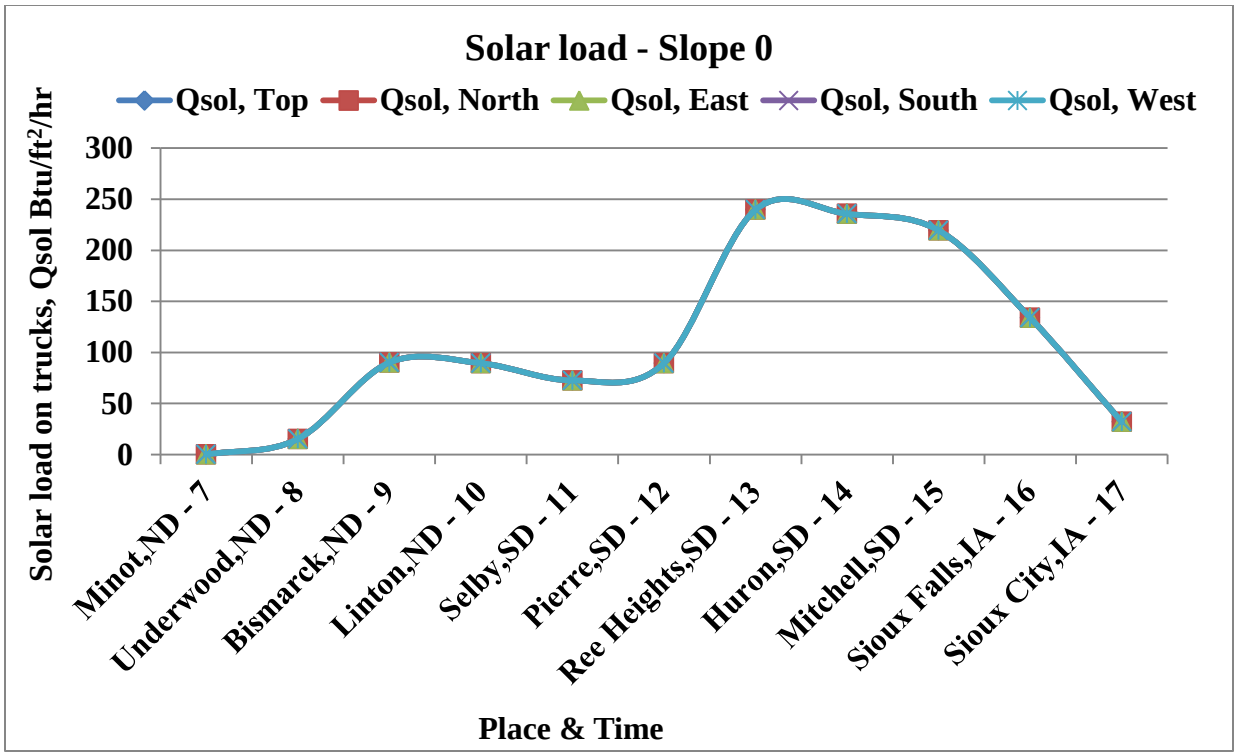

Figure 40: Solar load on the horizontal surface of the truck during a day in spring season (Minot, ND to Sioux City, IA)

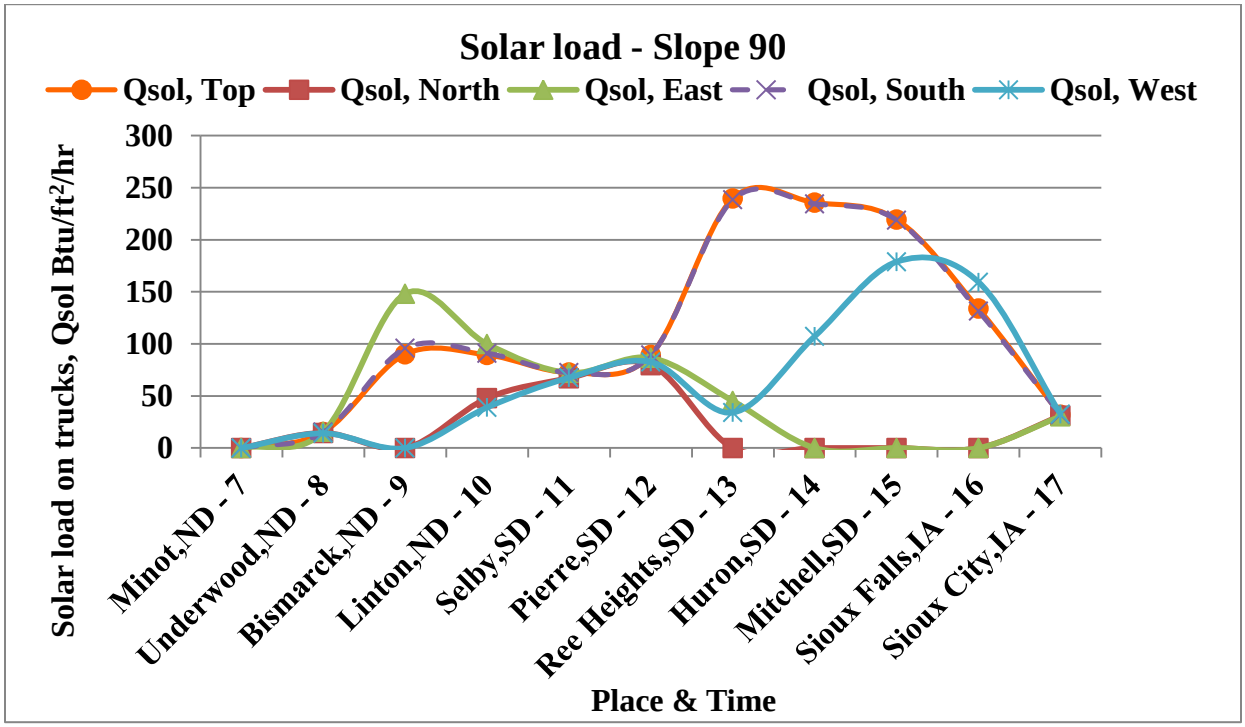

Figure 41: Solar load on the vertical surface of the truck during a day in spring season (Minot, ND to Sioux City, IA)

c. **Summer and winter seasons:** Figures 42 to 45 show a drastic change in solar load on the surfaces of the truck due to two contrasting seasons (summer and winter). From Figures 43 and 44 it can be observed that the solar load on the top surface of the truck reached a maximum value of $300\ \mathrm{Btu/ft^2/hr}$ ($946\ \mathrm{W/m^2}$) during summer at Ree Heights by 1 PM. From this calculated solar load, it can be understood that zero sky cover and low elevation have contributed to a relatively high solar load. For the truck travel from Linton, ND (10 AM) to Selby, SD (11 AM), there was a steep increase in solar load of top surface of the truck. This was due to complete cloud cover at Linton, ND and clear sky at Selby, SD. The solar load was maintained almost at the same level of $300\ \mathrm{Btu/ft^2/hr}$ ($946\ \mathrm{W/m^2}$) during the truck travel from Pierre (12 PM) to Mitchell (3 PM) due to same cloud cover. In winter, the maximum solar load on top surface of the truck was just $66\ \mathrm{Btu/ft^2/hr}$ ($208\ \mathrm{W/m^2}$) at Pierre by 12 PM, which has high total and opaque sky cover of nine. The south surface of the truck received a solar load of $78\ \mathrm{Btu/ft^2/hr}$ ($246\ \mathrm{W/m^2}$) and the other surfaces of the truck received lesser amount of solar load, when compared to the south surface. Figures 42, 43, 44 and 45 show the solar load on the horizontal and vertical surfaces of the truck during a day in summer and winter seasons (Minot, ND to Sioux City, IA).

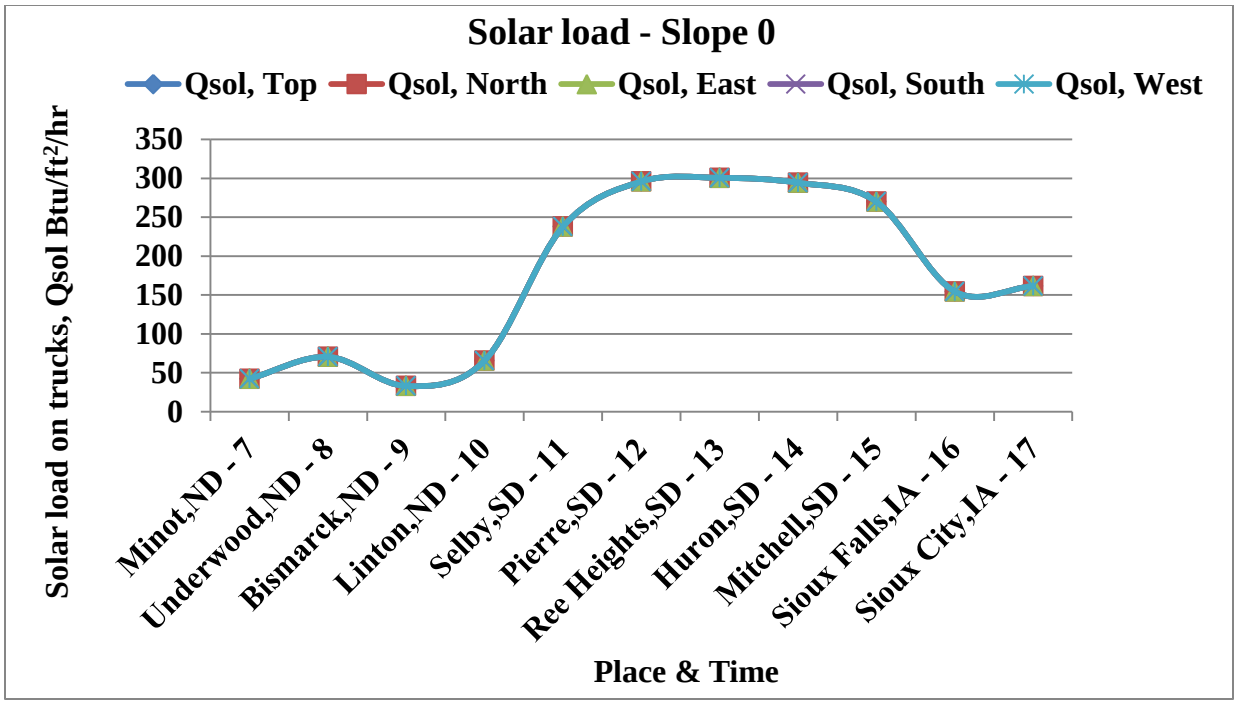

Figure 42: Solar load on the horizontal surface of the truck during a day in summer season (Minot, ND to Sioux City, IA)

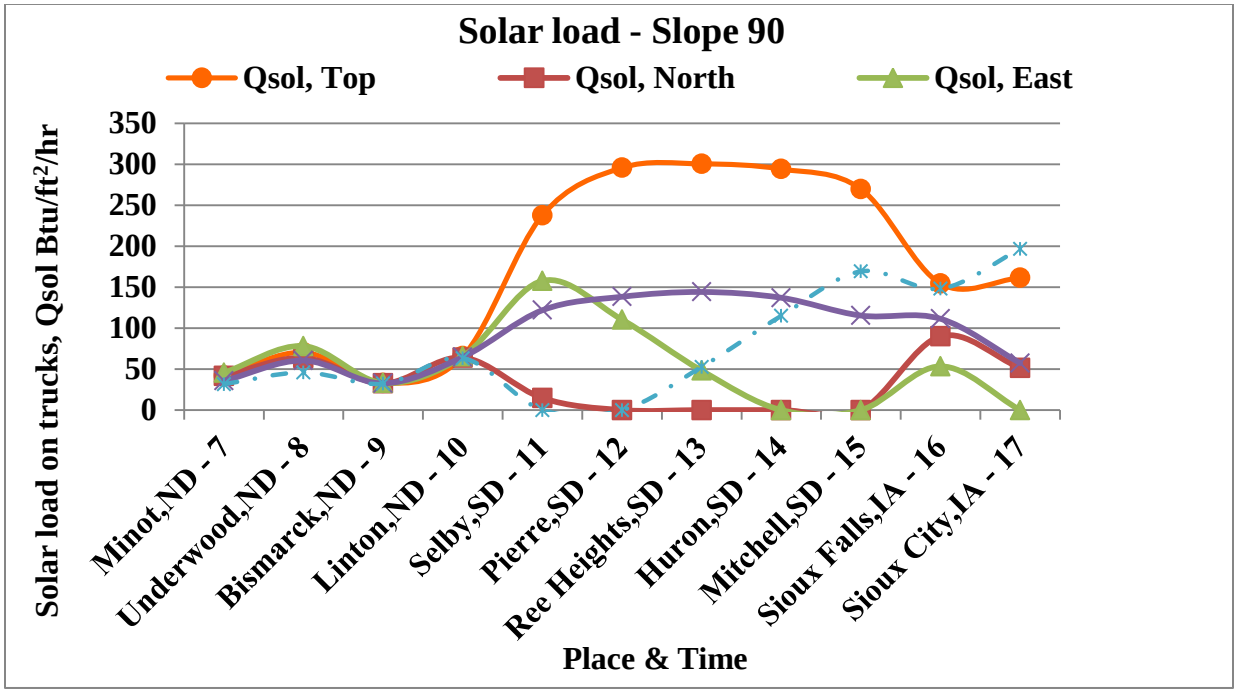

Figure 43: Solar load on the vertical surface of the truck during a day in summer season (Minot, ND to Sioux City, IA)

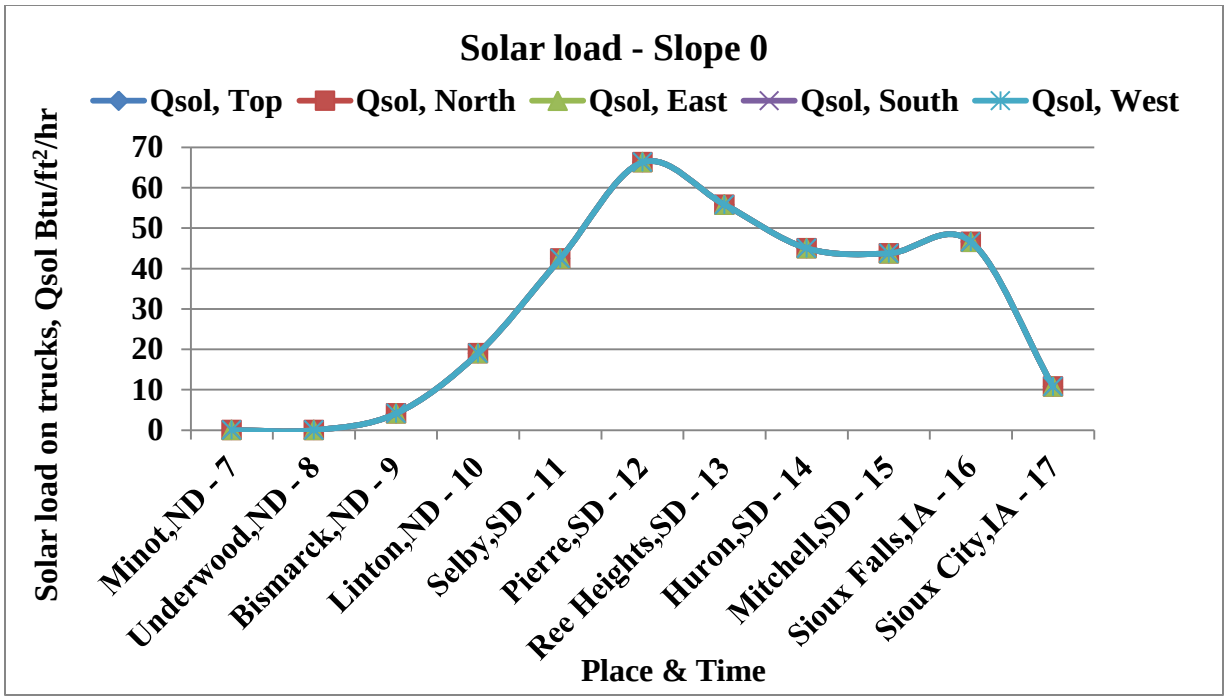

Figure 44: Solar load on the horizontal surface of the truck during a day winter season (Minot, ND to Sioux City, IA)

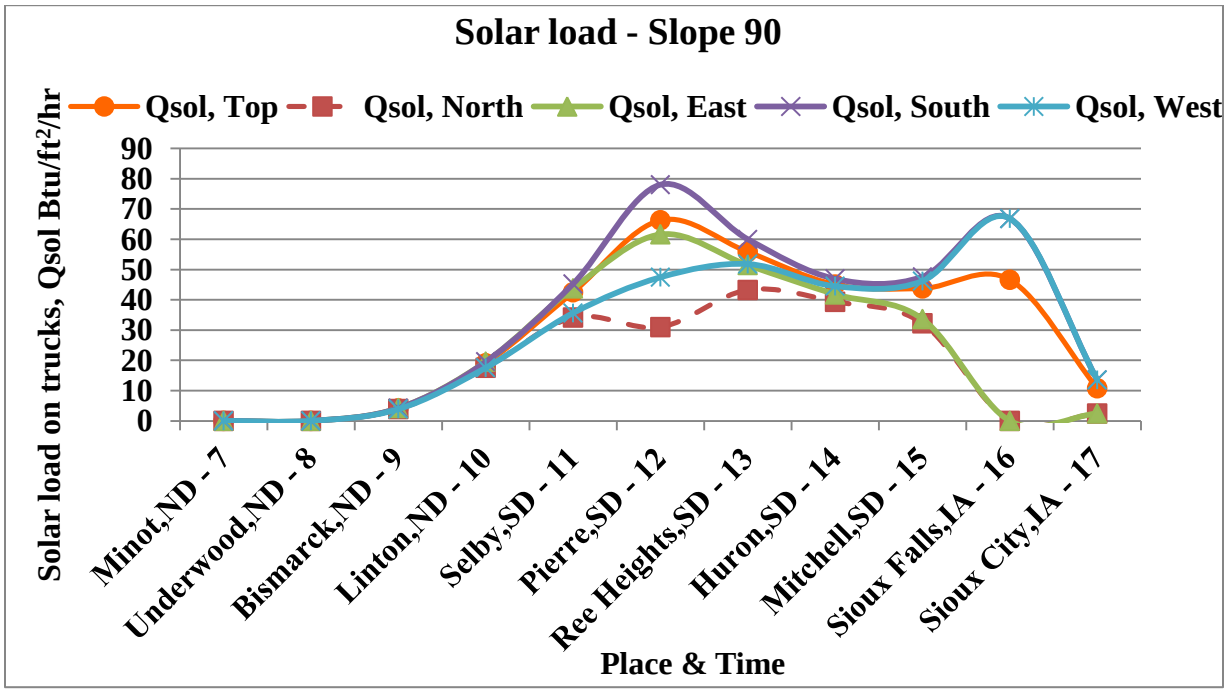

Figure 45: Solar load on the vertical surface of the truck during a day in winter season (Minot, ND to Sioux City, IA)

2. **Solar loads – Sacramento, CA to San Diego, CA:** Plots presented in Figures 46 through 53 depict the solar load for both horizontal and vertical surfaces of the truck for the Sacramento, CA to San Diego, CA route.

   a. **Fall season:** Figures 46 and 47 show the solar load on the surfaces of the truck during fall season. The solar load on the top surface of the truck was $133\ \text{Btu/ft}^2/\text{hr}\ (419\ \text{W/m}^2)$ at Sacramento by 9 AM. This value was relatively high, when compared to the solar load value of Minot, ND to Sioux City, IA route for 9 AM. There was a variation in solar load on top surface of the truck and the solar load reached a maximum value of $208\ \text{Btu/ft}^2/\text{hr}\ (656\ \text{W/m}^2)$ by 12 PM at Tracy, CA and was maintained constantly at the same level until 3 PM. These calculated solar loads show that even if sky as is completely domed by clouds (total and opaque sky cover of ten), a elevation (as low as 2 meters or 6.5 ft) above sea level, could result in high solar loads. Once the truck reached Boron by 6 PM, the solar load on the top surface reduced to zero. On the other hand, the solar load on the east surface of the truck reached a maximum value of $241\ \text{Btu/ft}^2/\text{hr}\ (760\ \text{W/m}^2)$ at Sacramento, CA by 9 AM with zero sky cover and elevation of just 7 meters (23 ft) above sea level. It can be observed from Figure 47, that there was a sudden fall in solar load in the east surface of the truck from Sacramento, CA (9 AM) to Oakley, CA (10 AM). This was due to the difference in total and opaque sky cover between two stations, in spite of being at the same elevation. The solar load on the east surface gradually reduced as the sun moves across the sky towards the sunset point. The south surface of the truck was exposed to relatively low solar load as the truck started from north of the California state and eventually received

more load during noon. Figures 46 and 47 show the solar load on the horizontal and vertical surfaces of the truck during a day in fall season (Sacramento, CA to San Diego, CA).

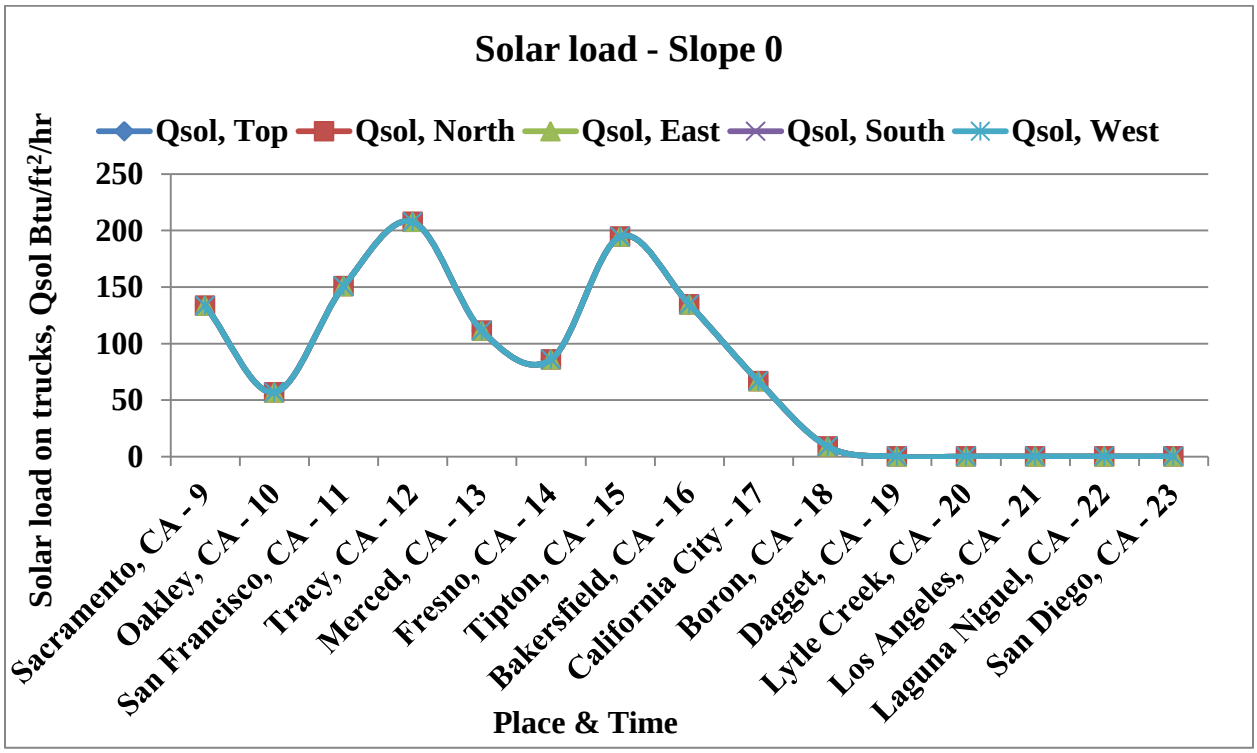

Figure 46: Solar load on the horizontal surface of the truck during a day in fall season (Sacramento, CA to San Diego, CA)

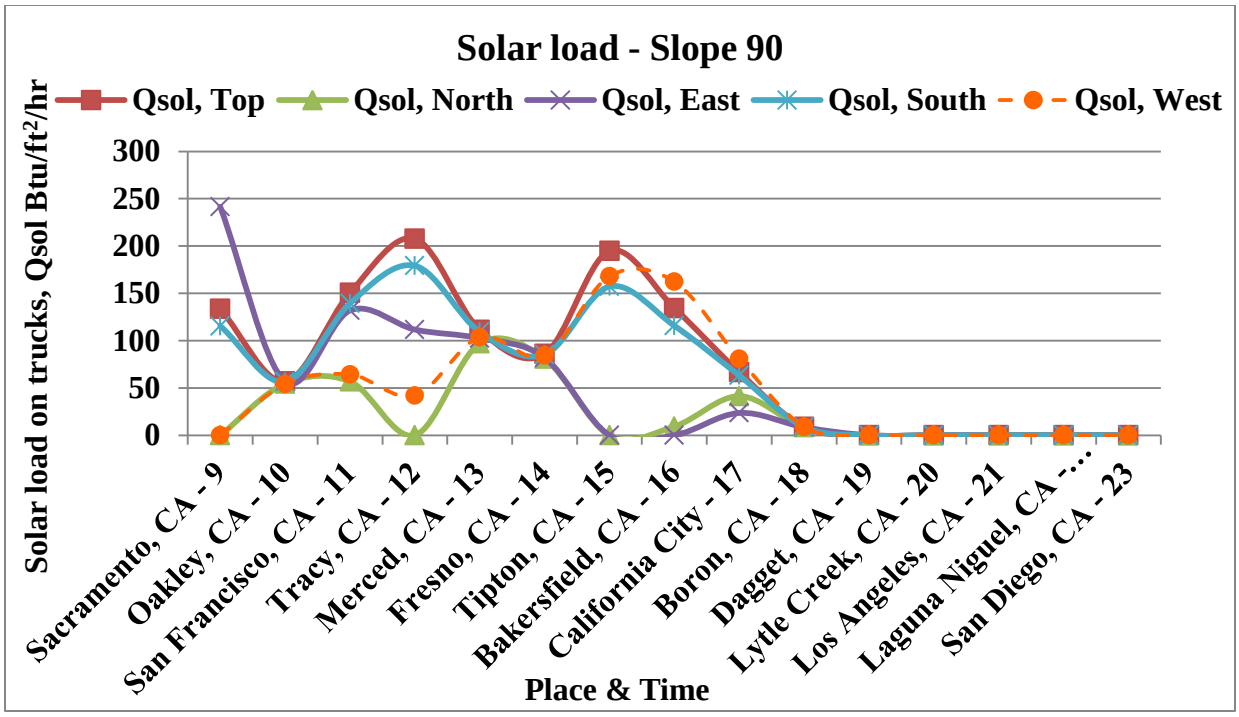

Figure 47: Solar load on the vertical surface of the truck during a day in fall season (Sacramento, CA to San Diego, CA)

b. Spring season: The solar load on horizontal and vertical surfaces of the truck during spring season was almost similar, when compared to the fall season. The top surface of the truck was exposed to solar load from 9 AM and reached a maximum value of 259 $\text{Btu/ft}^2\text{/hr}$ (816 W/m^2) at Tracy, CA by 12 PM with zero sky cover and elevation of just 2 meters (6.56 ft) above sea level. On the other hand, the north surface of the truck experienced a solar load of 48 $\text{Btu/ft}^2\text{/hr}$ (151 W/m^2). This value was relatively high, when compared to the solar load value of north surface of the truck during fall season. The south and east surface of the truck experienced a maximum solar load of 211 $\text{Btu/ft}^2\text{/hr}$ (665 W/m^2) at Tracy, CA by 12 PM and 237 $\text{Btu/ft}^2\text{/hr}$ (747 W/m^2) at Oakley, CA by 10 AM, with zero sky cover. Figures 48 and 49 show the solar load on various surfaces of the truck during a day in spring season (Sacrament, CA to San Diego, CA).

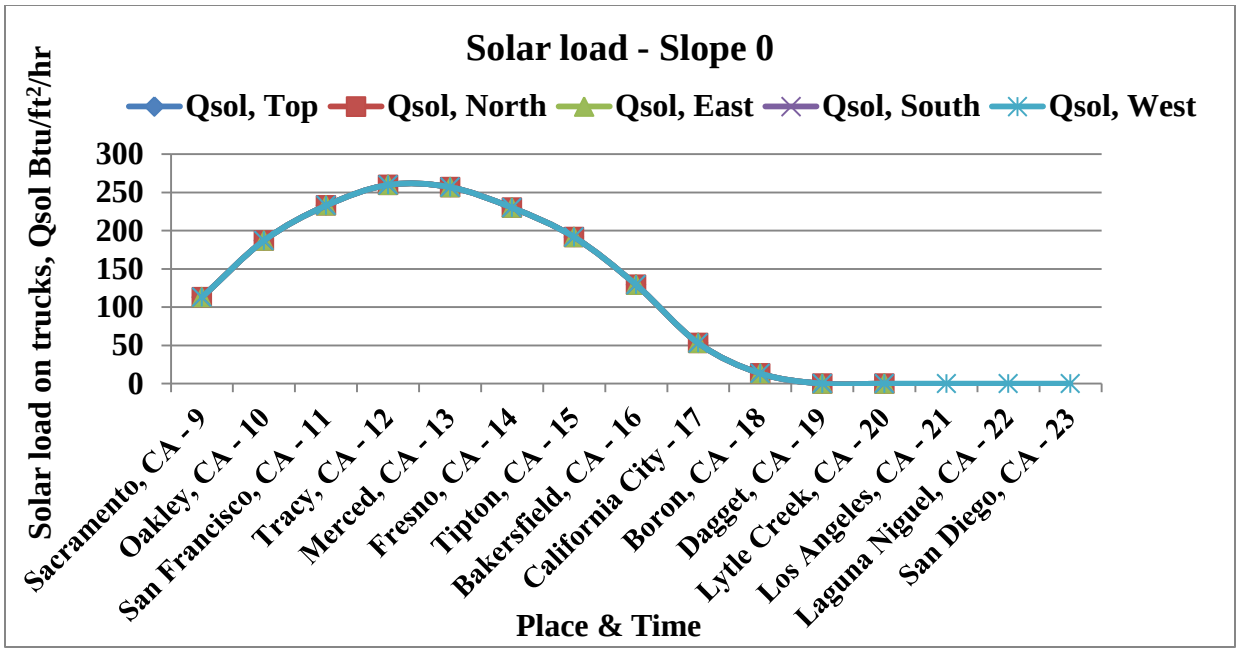

Figure 48: Solar load on the horizontal surface of the truck during a day in spring season (Sacramento, CA to San Diego, CA)

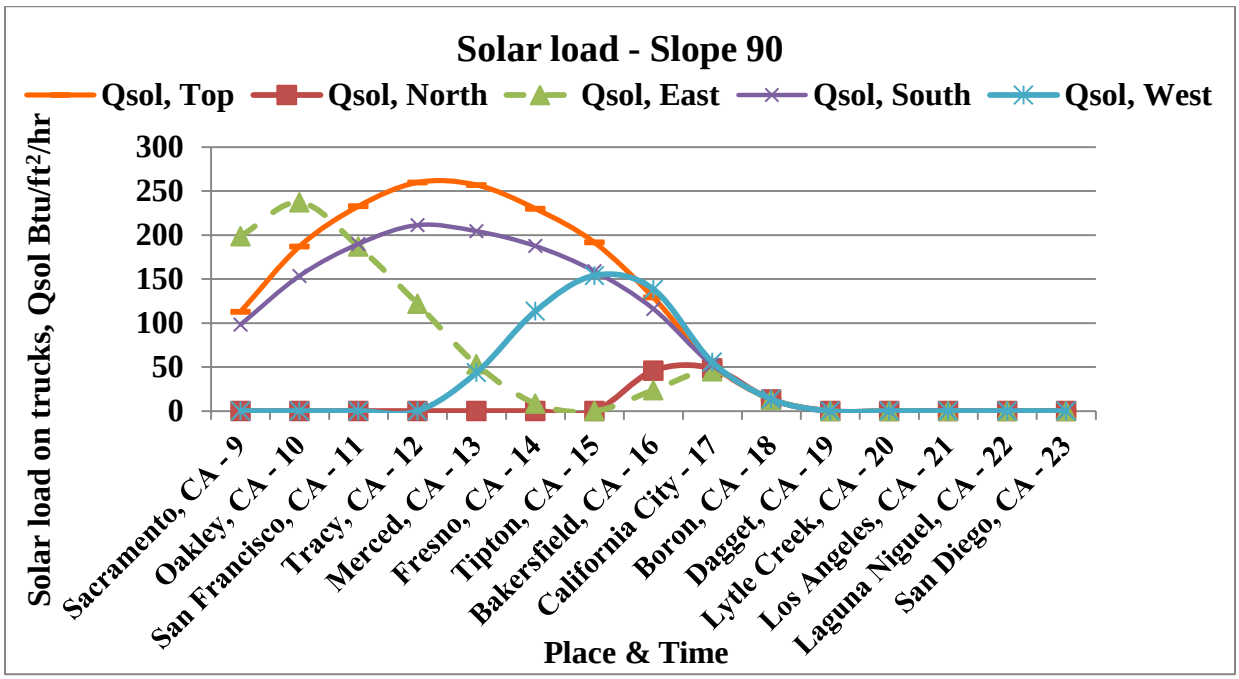

Figure 49: Solar load on the vertical surface of the truck during a day in spring season (Sacramento, CA to San Diego, CA)

c. **Summer and winter seasons:** Figures from 50 to 53 show the solar load on horizontal and vertical surfaces of the truck for summer and winter seasons. During summer season most of the intermediate locations between Sacramento, CA to San Diego, CA route had zero sky cover and low elevation, except Boron and Dagget, which resulted in high solar loads. For summer season, the solar load on top surface of the truck reached 198 Btu/ ft^2/hr (624 W/m^2) by 9 AM and further reached a maximum solar load of 314 Btu/ ft^2/hr (990 W/m^2) by 1 PM. This value was maintained until 4 PM, after which the solar load reduced to zero. On the other hand, the east surface of the truck received a maximum solar load of 245 $Btu/ft^2/hr$ (772 W/m^2) by 9 AM. The west surface of the truck started to experience solar load only by 12 PM, which is early, when compared to fall and spring season. There were a few fluctuations in the solar load from the west surface of the truck from Sacramento, CA (9 AM) to Tracy, CA (12 PM), in spite of having same cloud cover and elevation. These fluctuations could be attributed to parameters like atmospheric effects, absorption and scattering and variations in the atmosphere, and pollutions (global warming). In Sacramento, CA to San Diego, CA route the solar load during winter season showed a drastic change, when compared to Minot, ND to Sioux City, IA. The top surface of the truck received a maximum solar load of 149 $Btu/ft^2/hr$ (470 W/m^2) with zero sky cover, which is double the load value of top surface of the truck of Minot, ND to Sioux City, IA route. The south surface of the truck received a maximum solar load of 244 $Btu/ft^2/hr$ (770 W/m^2) with zero sky cover, which is almost thrice the solar load value of south surface of the truck of Minot, ND to Sioux City, IA route.

Figures 50, 51, 52 and 53 show the solar load on the vertical and horizontal surfaces of the truck during a day in summer and winter seasons (Sacramento, CA to San Diego, CA).

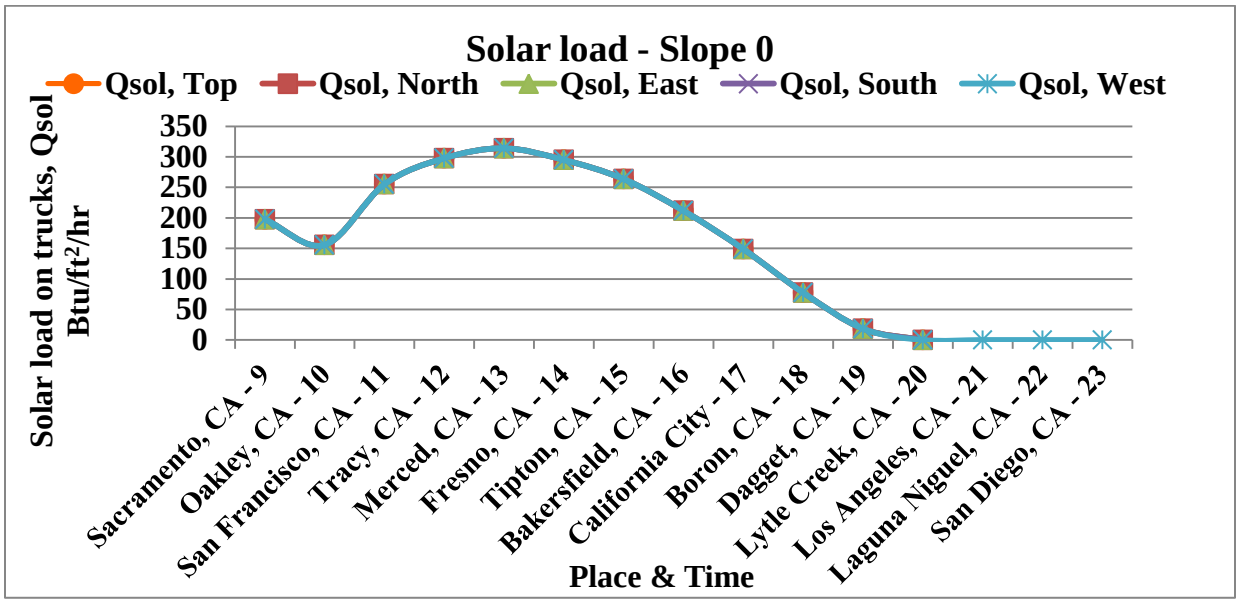

Figure 50: Solar load on the horizontal surface of the truck during a day in summer season (Sacramento, CA to San Diego, CA)

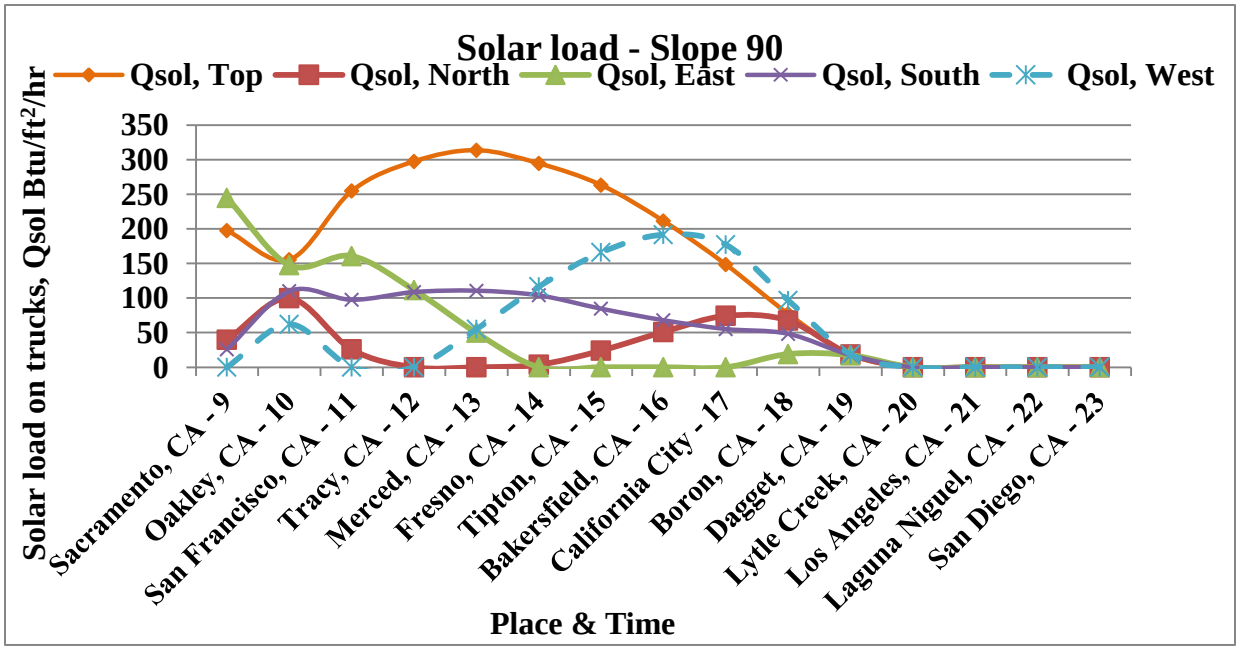

Figure 51: Solar load on the vertical surface of the truck during a day in summer season (Sacramento, CA to San Diego, CA)

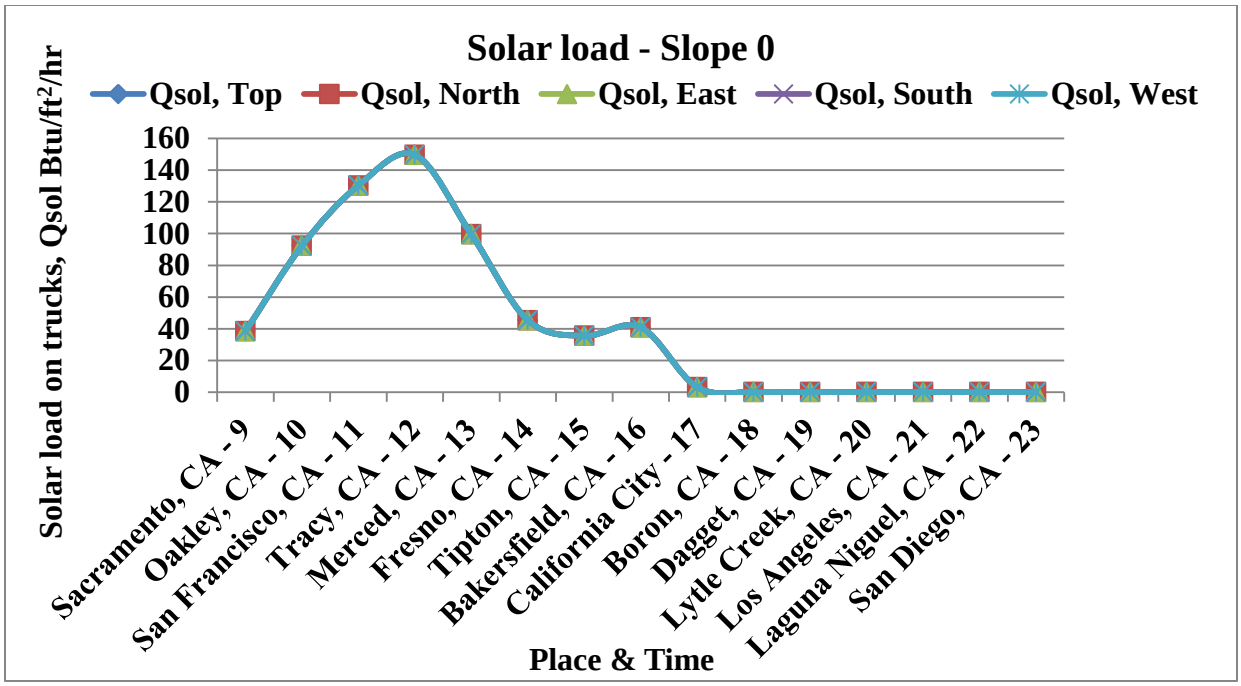

Figure 52: Solar load on the horizontal surface of the truck during a day in winter season (Sacramento, CA to San Diego, CA)

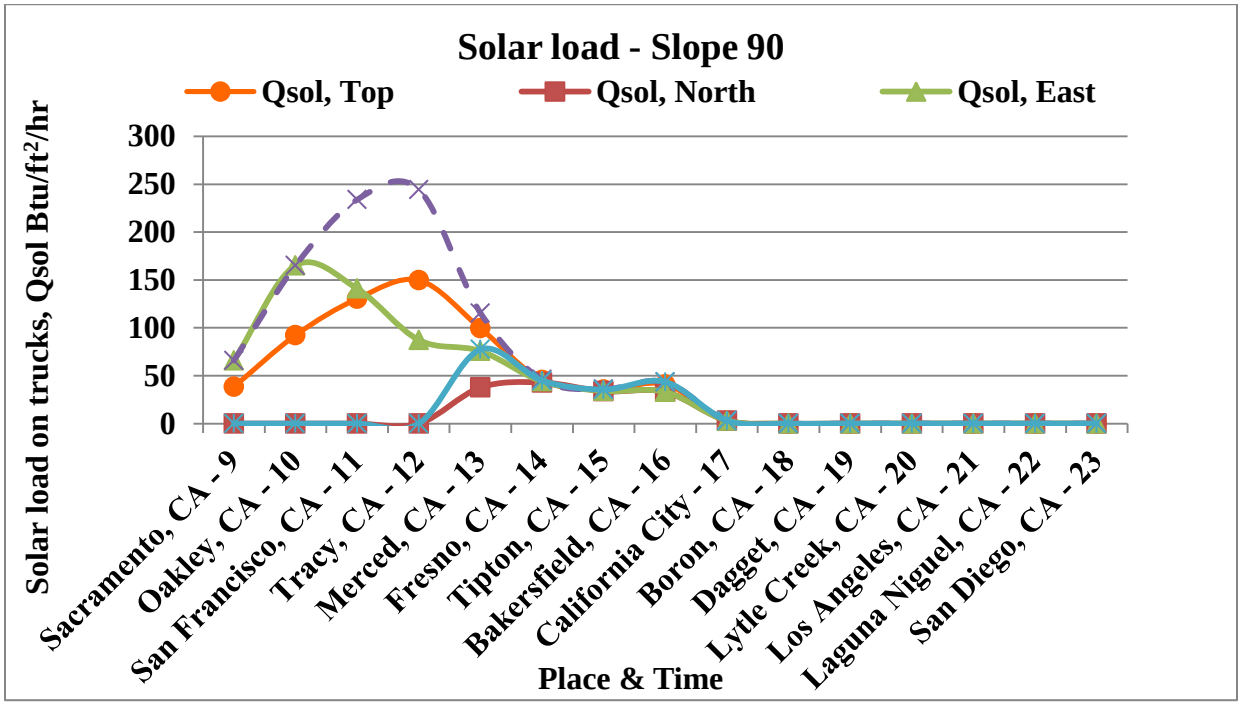

Figure 53: Solar load on the horizontal surface of the truck during a day in winter season (Sacramento, CA to San Diego, CA)

Wind chill temperature defined as the felt air temperature on exposed surface due to wind, similarly for the truck, wind chill temperature is the felt air temperature on the walls of the truck. Unlike solar loads, wind chill temperature is independent of cloud cover. However, recorded air temperature, wind speed have a major impact on the wind chill temperature. The actual effect of wind comes in to play, for the air temperatures at or below $50°F\ (10°C)$. Furthermore, other minor factors such as direction of the wind, relative humidity and speed of the truck also influence the wind chill temperature. In the following sections the effect of wind on air temperature for the different routes and seasons is presented:

3. **Wind chill temperatures – Minot, ND to Sioux City, IA:** Figures 54 to 57 explain the wind chill temperature on the walls of the truck for fall, spring, summer and winter season. For fall season, the wind chill temperature range varied from $44\ °F$ to $82\ °F\ (7°C$ to $28°C)$. By 12 PM, Pierre, SD recorded the maximum wind chill temperature of $82°F\ (28°C)$ during fall season due to maximum dry bulb temperature (air temperature), when compared to other intermediate stations. For spring season, the truck starting station Minot (7 AM) experienced a wind chill temperature of -$7.0°F\ (-22°C)$ due to high wind speed as well as low dry bulb temperature. There was a steep increase in wind chill temperature between Underwood, ND (8 AM) and Bismarck, ND (9 AM) due to sudden decrease in wind speed. As the truck traveled farther, the wind chill temperature reached a maximum value of $57\ °F\ (14°C)$ at Sioux Fall, SD by 4 PM during spring season. For winter, the truck starting station Minot, ND recorded a minimum wind chill temperature of $-5.0°F\ (-21°C)$ due to high wind speed as well as minimum dry bulb temperature. In the summer, the maximum wind chill temperature was

66°F (19°C) by 7 AM and this value was maintained at the same level until 3 PM and further it reached a maximum value of 88 °F (31°C) .

Figures 54, 55, 56 and 57 show the wind chill temperatures on the walls of the truck for Minot, ND to Sioux City, IA route.

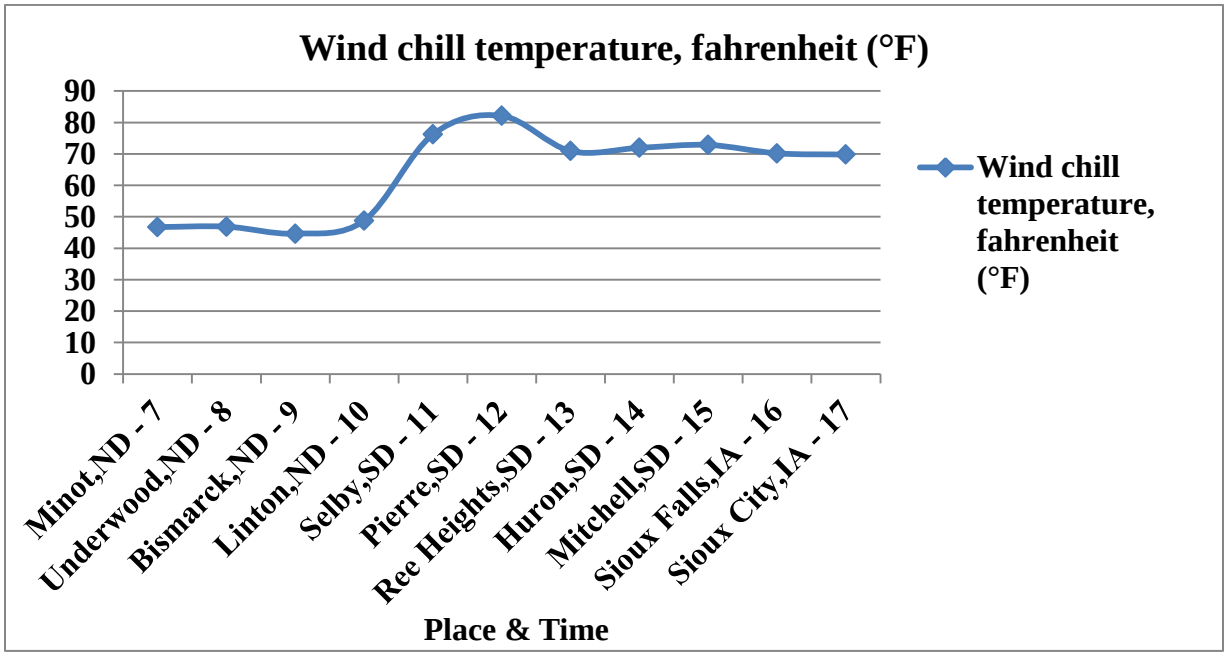

Figure 54: Wind chill temperatures on the walls of the truck during a day in fall season (Minot, ND to Sioux City, IA)

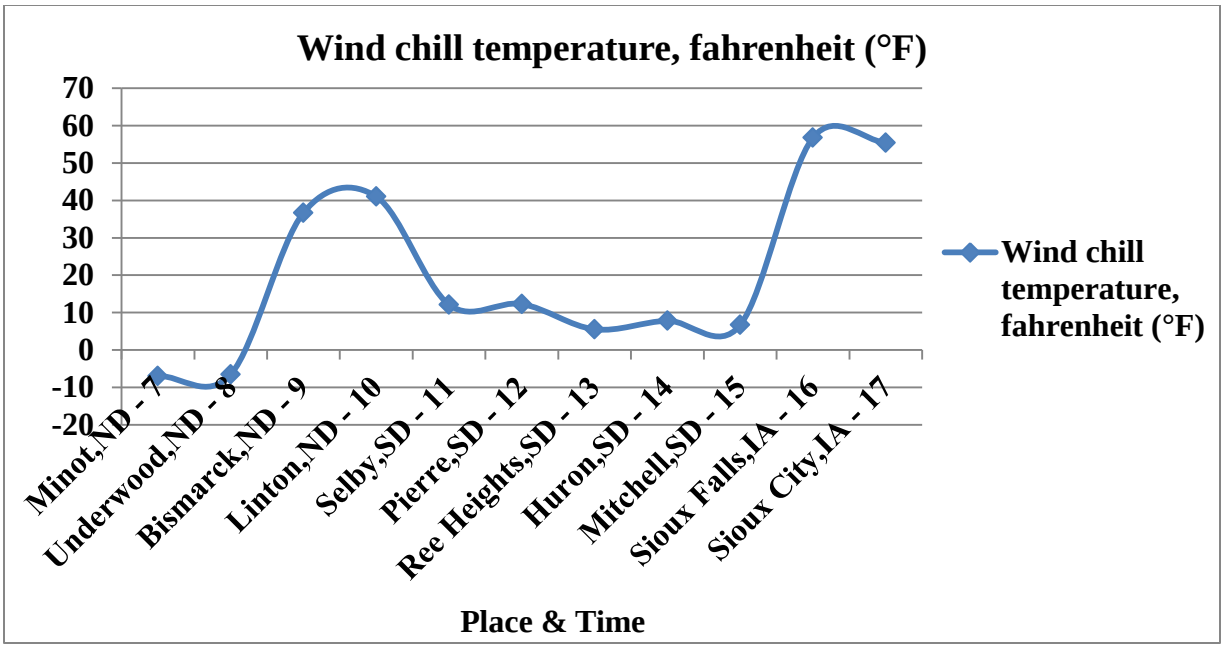

Figure 55: Wind chill temperatures on the walls of the truck during a day in spring season (Minot, ND to Sioux City, IA)

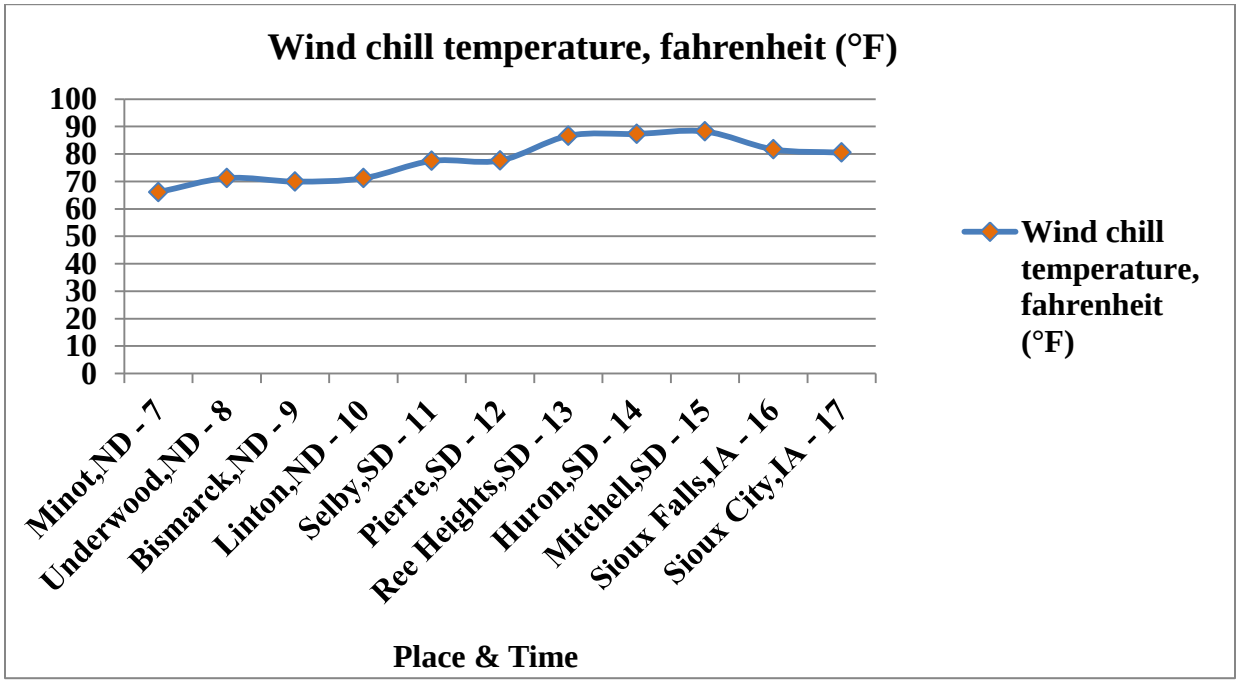

Figure 56: Wind chill temperatures on the walls of the truck during a day in summer season (Minot, ND to Sioux City, IA)

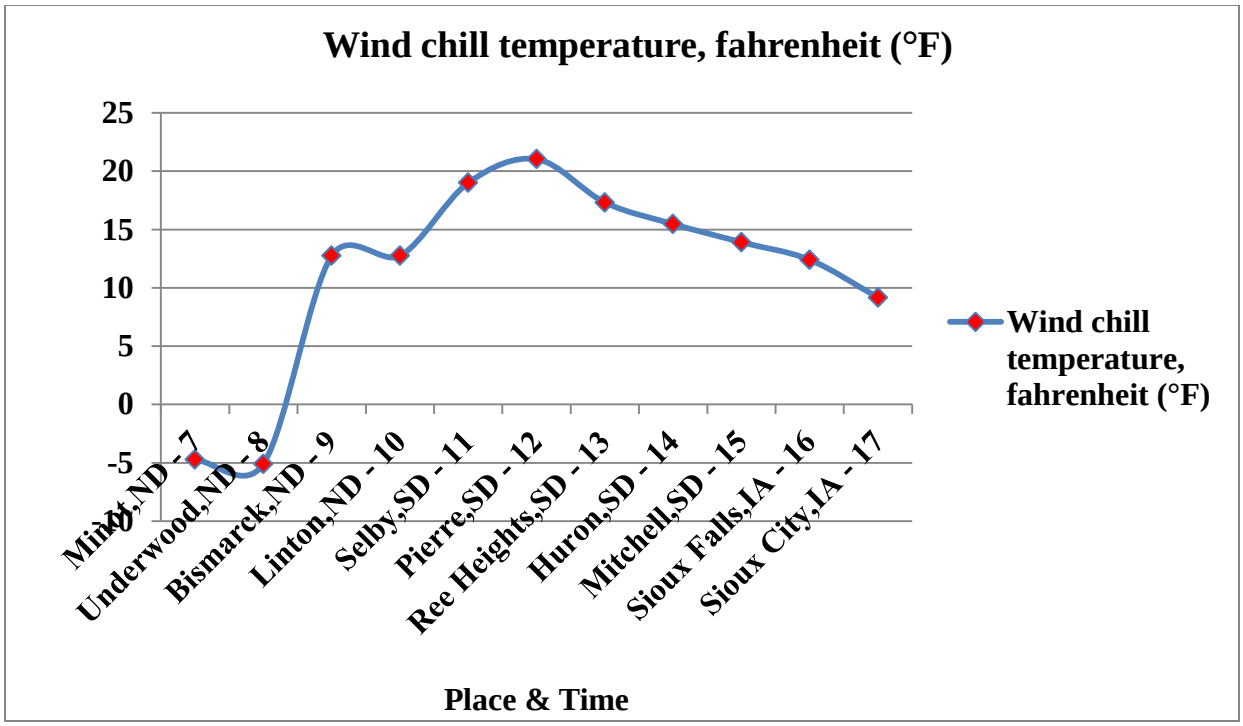

Figure 57: Wind chill temperatures on the walls of the truck during a day in winter season (Minot, ND to Sioux City, IA)

4. **Wind chill temperatures – Sacramento, CA to San Diego, CA:** The wind chill temperature of Sacramento, CA to San Diego, CA route is presented in Figures 58 through 61. All the intermediate stations of Sacramento, CA to San Diego, CA route recorded less wind speed and high dry bulb temperature, which resulted in maximum wind chill temperature, when compared to Minot, ND to Sioux City, IA route. Figure 59 depicts the wind chill temperature for fall season. While the wind chill temperature ranged from 64 °F to 99 °F (18°C to 37°C) during fall. The truck recorded a maximum wind chill temperature of 99°F (37°C) at Bakersfield by 4 PM, due to high dry bulb temperature (air temperature), when compared to other intermediate stations. During spring, the wind chill temperature varied between 53 °F and 84 °F (12°C and 29°C). There was a sudden increase in wind chill temperature from California City, CA (5 PM)

to Lytle Creek, CA (8 PM), due to variation in dry bulb temperature (air temperature) in wind speed between the intermediate locations. In summer, the truck recorded a maximum wind chill temperature of 103 °F (39°C). During winter, it varied between 41 °F and 71 °F (5°C and 22°C) which is quiet high, when compared to wind chill temperature of Minot, ND to Sioux City, IA. Figures 58, 59, 60, 61 show the wind chill temperatures on the walls of the truck for Sacramento, CA to San Diego, CA route.

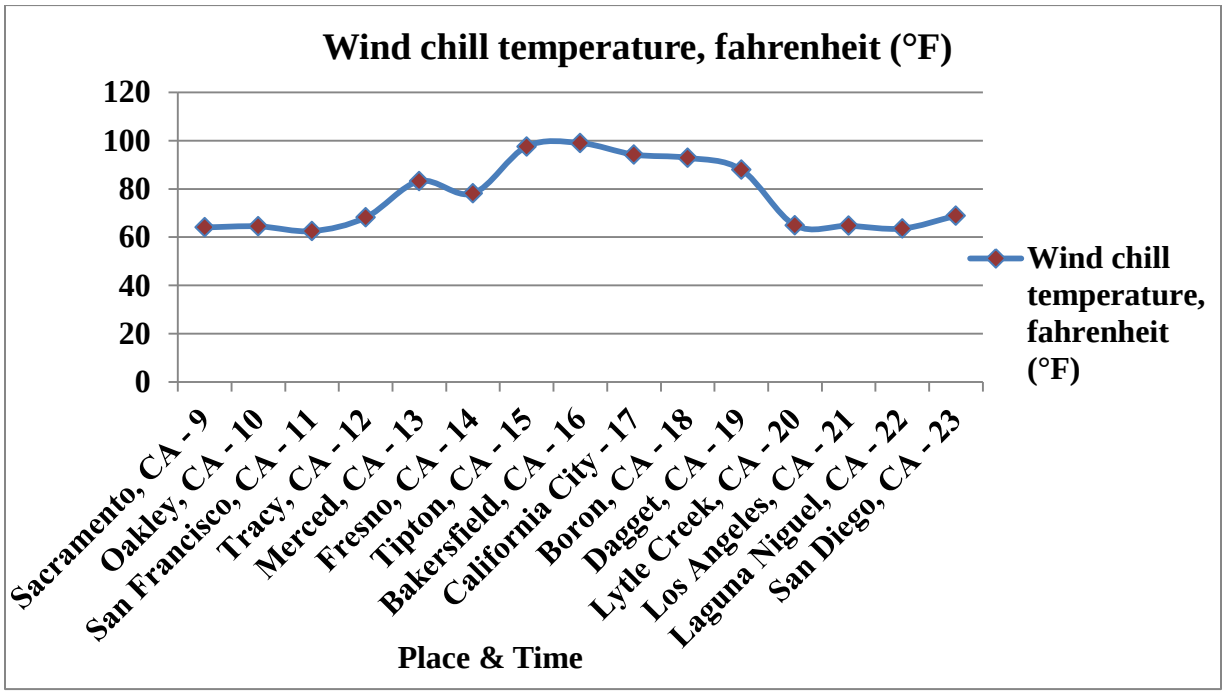

Figure 58: Wind chill temperatures on the walls of the truck during a day in fall season (Sacramento, CA to San Diego, CA)

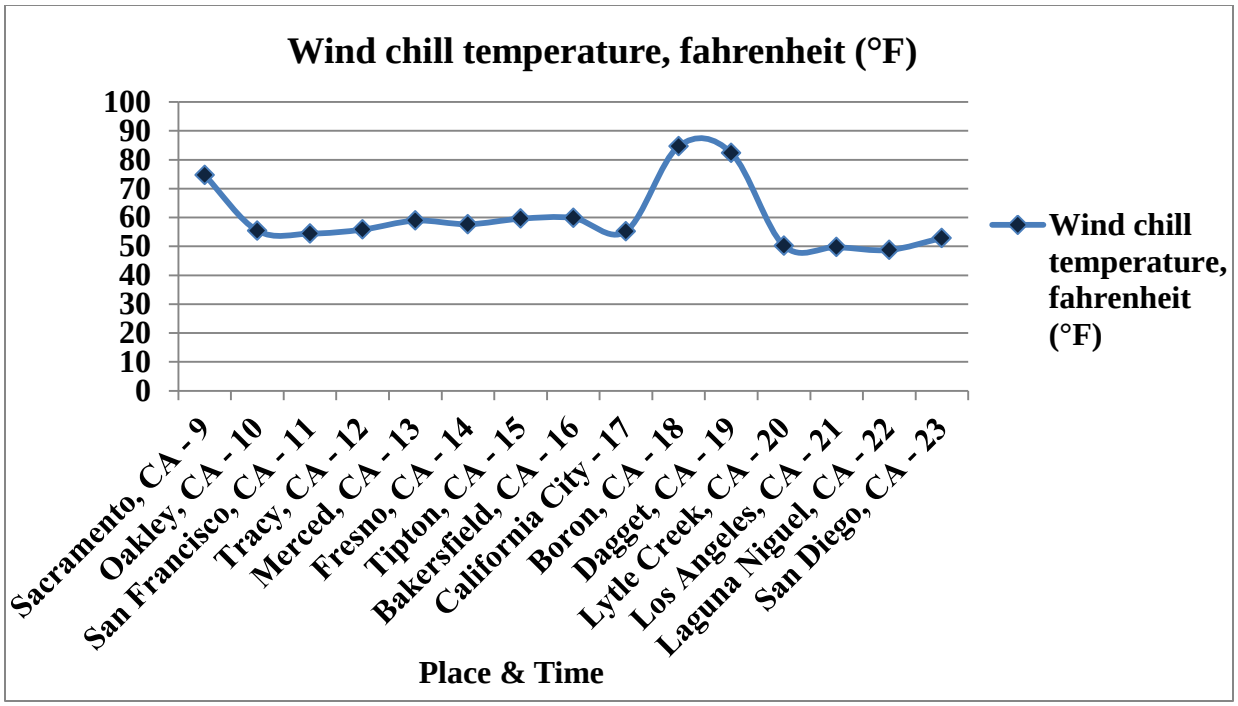

Figure 59: Wind chill temperatures on the walls of the truck during a day in spring season (Sacramento, CA to San Diego, CA)

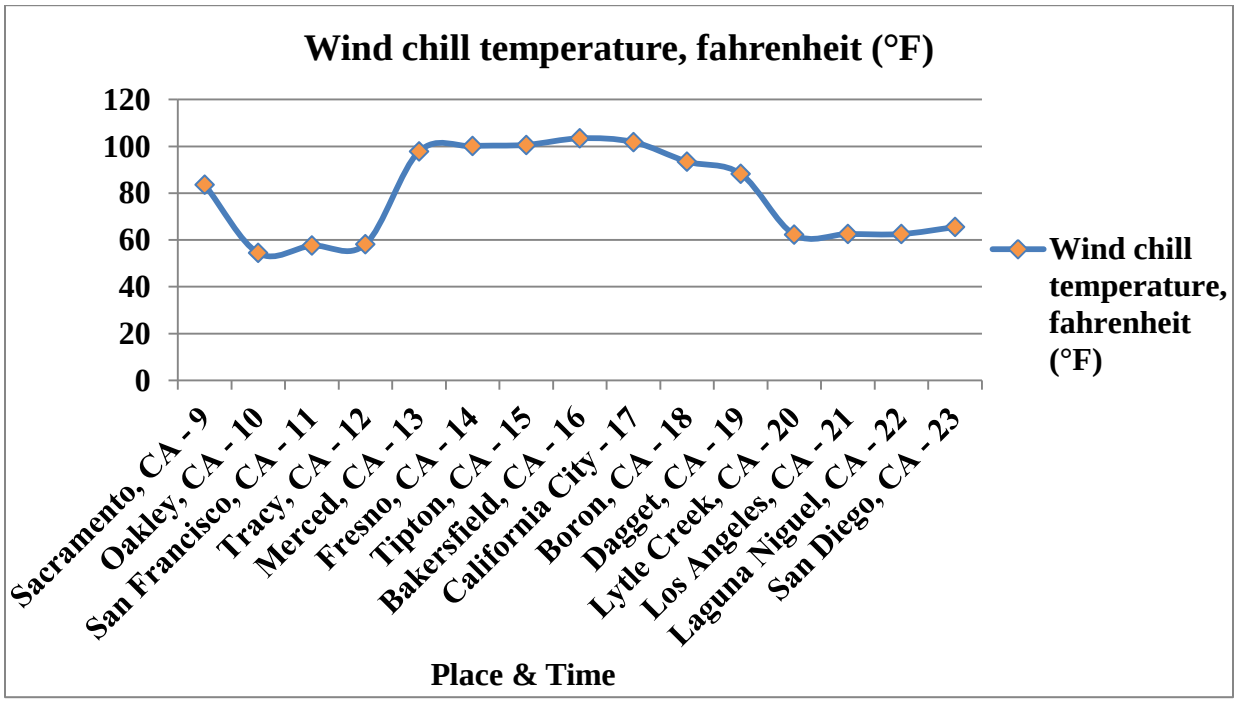

Figure 60: Wind chill temperatures on the walls of the truck during a day in summer season (Sacramento, CA to San Diego, CA)

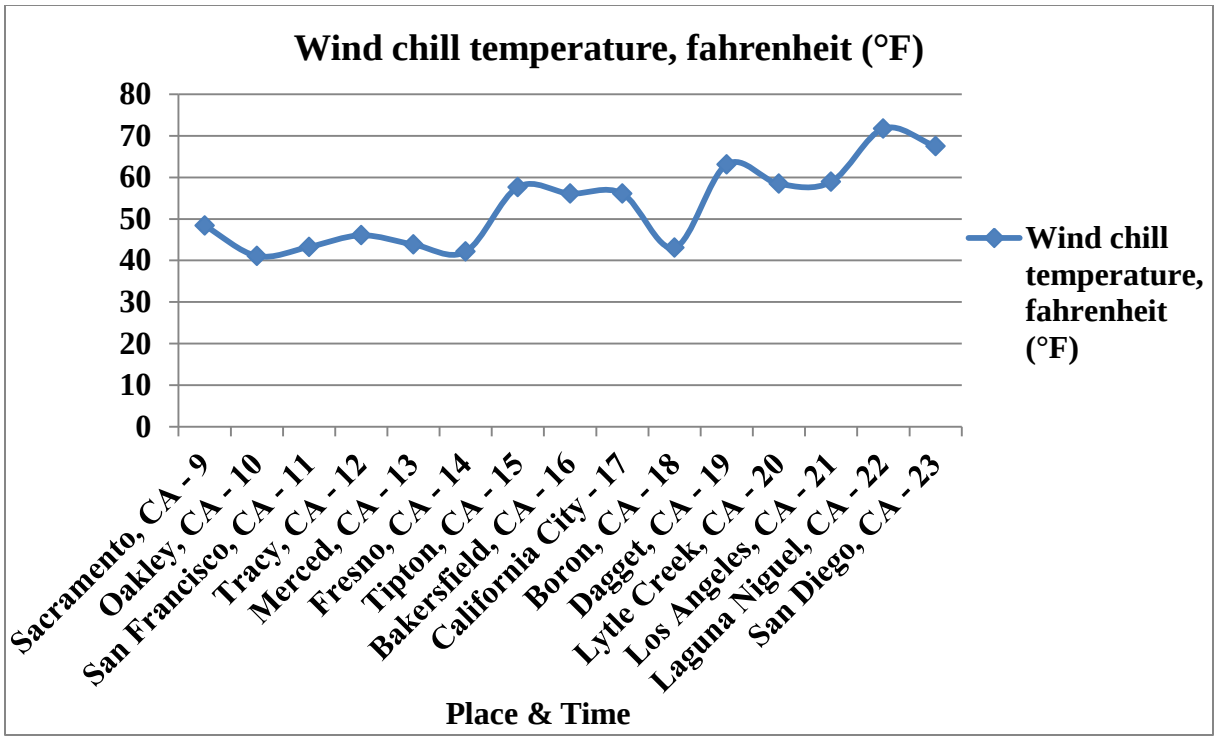

Figure 61: Wind chill temperatures on the walls of the truck during a day in winter season (Sacramento, CA to San Diego, CA)

The interior surface temperatures of the refrigerated tractor trailers were primarily affected by recorded solar loads, air temperatures, and truck outside surface temperatures. Furthermore, other factors such as sky temperatures, absorptivity's and emissivity's of the truck construction material and the insulation material placed between the truck walls also influenced the interior surface temperatures of the truck. The following results show the behavior of interior surface temperatures for summer and winter.

5. Quasi-steady state heat transfer across the walls of refrigerated tractor trailer – Minot, ND to Sioux City, IA: The interior surface temperature of Minot, ND to Sioux City, IA route is presented in Figures 62 and 63. For winter season, all the surfaces of the truck experienced low interior surface temperature of around $-3°F\,(-19℃)$ at Minot and Underwood. The east surface of the truck experienced a low interior surface temperature of $-5.0°F\,(-21℃)$ at Underwood by $8\ AM$ due to zero incoming solar radiation and low air temperature of $-2.0°F(-19.0℃)$. After this, there was a steep increase in interior surface temperatures for all the surfaces. The south surface of the truck experienced a maximum interior surface temperature of $36°F(2.0℃)$ at Pierre by 12 PM due to high incoming solar radiation of $66.27\ \mathrm{btu/ft^2/hr}\ (209\ \mathrm{W/m^2})$ and high air temperature of 34°F (1℃). For summer season, the top surface of the truck experienced a maximum interior surface temperature of $100°F(38℃)$ at Huron, SD by 2 PM, due to high incoming solar radiations and high air temperature. Figures 62 and 63 show the interior surface temperatures on the walls of the truck for Minot, ND to Sioux City, IA route.

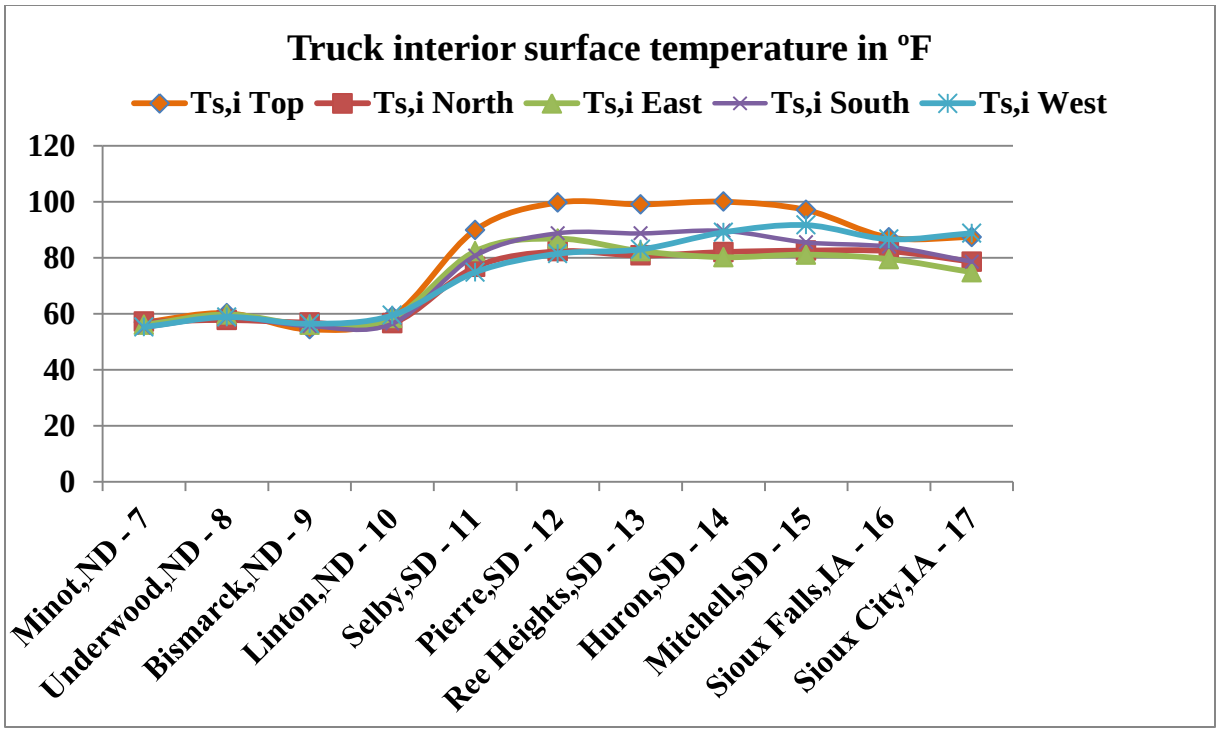

Figure 62: Interior surface temperatures on the walls of the truck during a day in summer season (Minot, ND to Sioux City, IA)

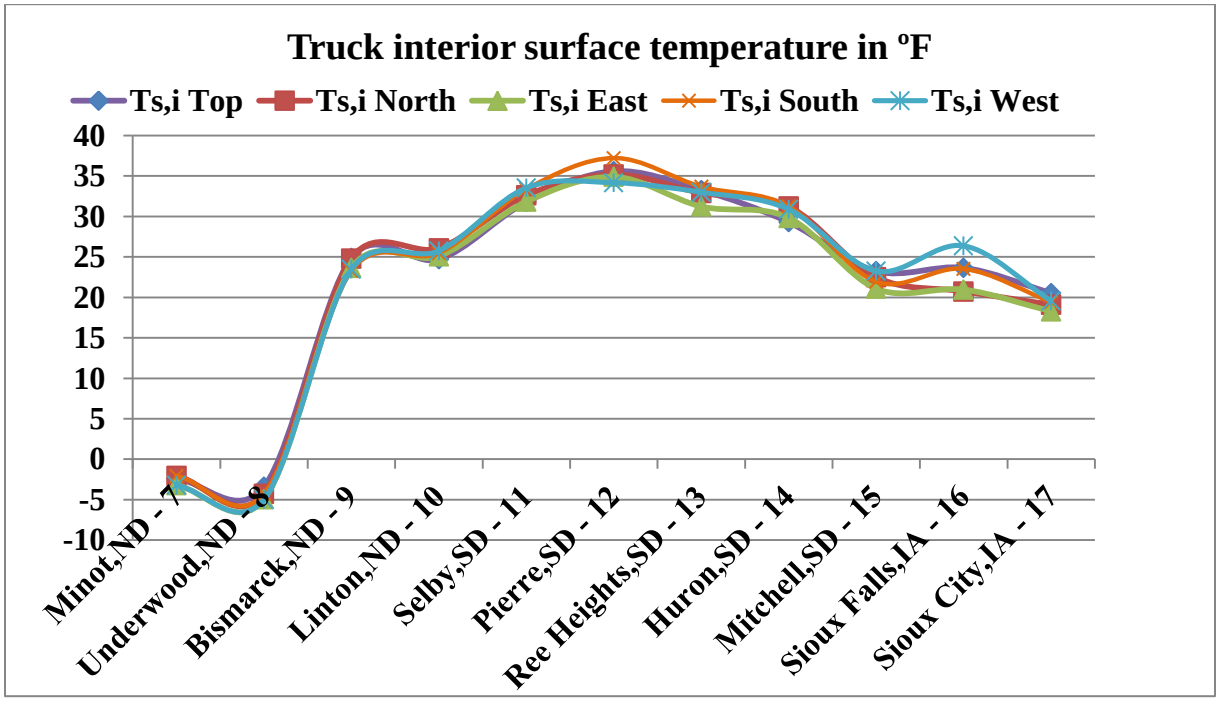

Figure 63: Interior surface temperatures on the walls of the truck during a day in winter season (Minot, ND to Sioux City, IA)

6. Quasi-steady state heat transfer across the walls of refrigerated tractor trailer – Sacramento, CA to San Diego, CA: The interior surface temperatures of Sacramento, CA to San Diego, CA route is presented in Figures 64 and 65. All the intermediate stations of Sacramento, CA to San Diego, CA route recorded high solar load and dry bulb temperature, which resulted in high interior surface temperatures, when compared to Minot, ND to Sioux City, IA route. Figure 64 depicts the interior surface temperatures on all the surfaces of the truck for summer season. The top surface of the truck experienced high interior surface temperature of $108°F(42°C)$ due to high solar load of $264\ Btu/ft^2/hr\ (832\ W/m^2)$ and high dry bulb temperature of $93°F(34°C)$ which is quite high when compared to Minot, ND to Sioux City, IA for summer season. In winter, the south surface of the truck experienced high interior surface temperature of $62°F(17°C)$ which is double the value of Minot, ND to Sioux City, IA route and high interior surface temperature is due to high solar load of $244.35\ Btu/ft^2/hr\ (770\ W/m^2)$ and high dry bulb temperature of $52°F(11°C)$. Figures 64 and 65 show the interior surface temperatures on the walls of the truck for Sacramento, CA to San Diego, CA route.

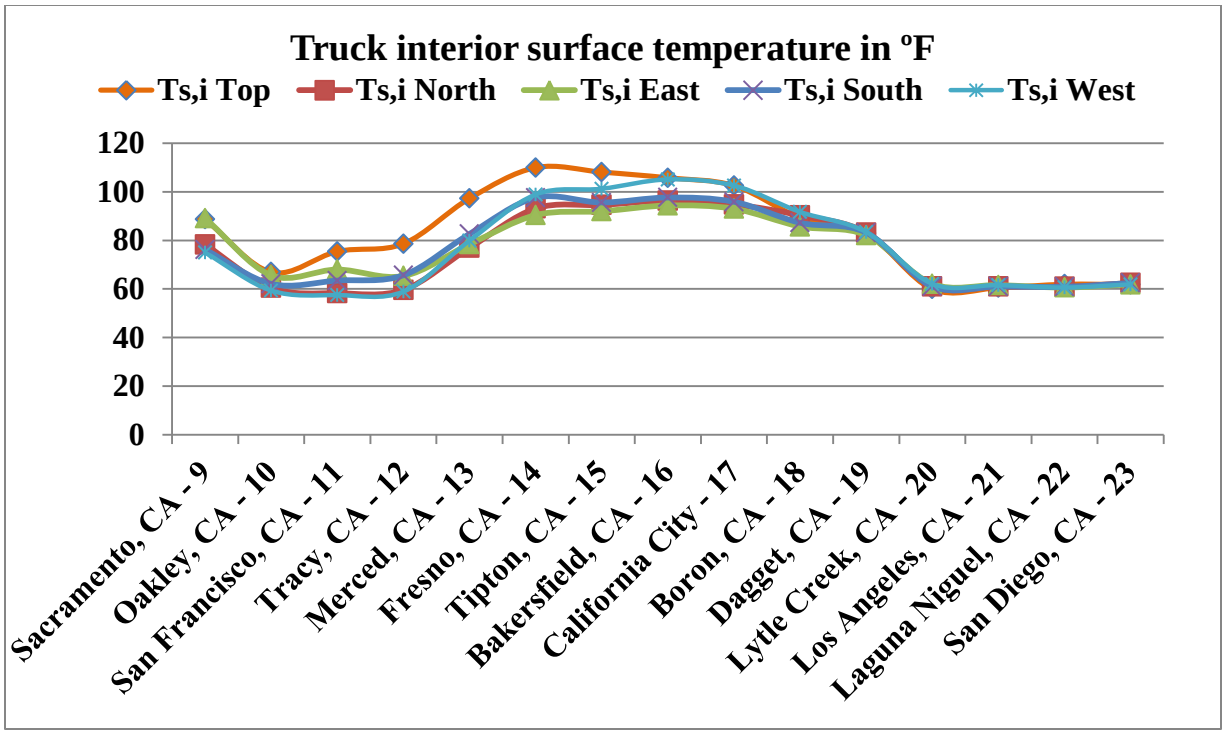

Figure 64: Interior surface temperatures on the walls of the truck during a day in summer season (Sacramento, CA to San Diego, CA)

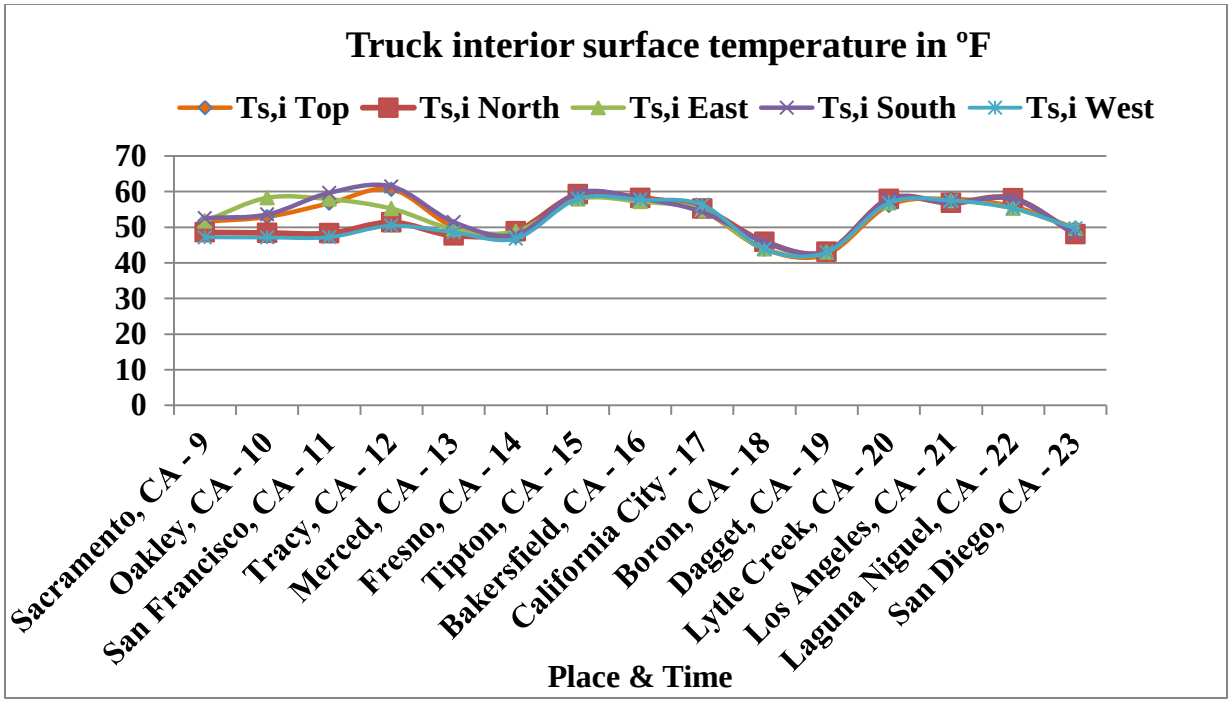

Figure 65: Interior surface temperatures on the walls of the truck during a day in winter season (Sacramento, CA to San Diego, CA)

Chapter VIII: Conclusions and future work

Conclusions

This research work presented a technique to calculate solar loads, wind chill temperatures and interior surface temperatures on the surfaces of moving refrigerated tractor trailers outfitted with phase change materials, based on synthesized weather data obtained from the National Solar Radiation Data Base (NSRDB).

In this research work, eight different routes running across the Continental United States covering different weather conditions were selected. This study on solar load, wind chill temperature and interior surface temperature reveals the following:

- The solar load, wind chill temperatures and interior surface temperature recorded from the walls of the truck surface follow a trend based on the season of the year, time of the day, direction of the surface with respect to the Sun, location of the route.
- There are other parameters too such as cloud cover and elevation that influence solar load recorded. In addition to this minor factors such as atmospheric effects, absorption and scattering and variations in the atmosphere, and pollutions (global warming) which result in minor fluctuations in the data.
- The factors that influence the interior surface temperatures of the truck were recorded solar loads, air temperatures, truck outside surface temperatures, sky temperatures, absorptivity's and emissivity's of the truck construction material and the insulation material placed between the truck walls.
- Wind chill is primarily affected by wind speed, season of the year, with minor factors such as direction of the wind, relative humidity and speed of the truck.

The implications of this study are multifold. They are: 1) the recorded solar load, wind chill temperature and hourly heat balance at each of the routes is one of the vital parameters in selecting the appropriate PCM. 2) the varying levels of solar load on each of the walls helps in adjusting the quantity of PCM needed. 3). the interior surface temperatures of the truck would indicate, if the PCM will be melting or solidifying.

PCMs are one of the best available energy storage mediums, and their impact on heat transfer reduction was evident from the research work done at the University of Kansas. With the help of PCMs, the indoor of the trailers will experience less temperature swing; more stable operation, longer life and reduction in CO_2 emission. Therefore, PCMs can be termed as a 'Green' solution to the existing fuel hungry trucks. Another advantage of using a PCM system, when compared to several types of refrigeration cooling systems such as diesel driven, hydraulic drive unit and eutectic system is that the PCM system need not be charged periodically. Therefore a PCM system might be preferred over other refrigeration system, even if the cost benefit analysis is taken in to account. To this end, the usage of PCMs in moving refrigerated tractor trailers undergoing dynamic conditions was studied. The analysis done in this research, based on solar load and wind chill temperature on all the surfaces of the truck, provide a strong motivation towards using PCMs in moving tractor trailers.

Future work

There are several recommendations for future researches for this field:

- This research is an ongoing work, and there is plenty of scope for future work and improvement. It is assumed that the truck in its journey is aligned along one of the four cardinal directions (north, south, east and west). However, due to the curved nature of the route, the truck is not always aligned along the cardinal directions. This will

introduce significant differences in solar load calculation if done in reality. Therefore, the solar model can be improvised by estimating the solar load of the truck based on the exact orientation of the truck. This study used two weather data sets TMY2 data and TMY3 data. However, there is a need for a richer weather database which includes all intermediate stations between routes.

- The study on solar loads, wind chill temperatures and interior surface temperatures are some of the necessary conditions, but not sufficient for selecting the appropriate PCM and its quantity on each walls of the truck**.** PCM selection also depends on various other parameters like construction of the truck, types of goods transported, indoor temperature requirement and the PCM placement on the walls. The proposed solar model needs to be validated with field experiments. However, it is not feasible to conduct exhaustive field study and therefore, simulation experiments serve as an appropriate substitution.

Finally, this research work has opened a novel method for the future in saving energy consumption by refrigerated truck trailers outfitted with PCMs. This research idea can be taken to a wider range of audiences including private and public sectors, which might eventually utilize the results and recommendations presented in this research work.

References

1. Medina, M. A., J. B. King, et al. (2008). "On the heat transfer rate reduction of structural insulated panels (SIPs) outfitted with phase change materials (PCMs)." Energy 33(4): 667-678.
2. King JB. Preliminary Evaluation of the Thermal Performance of Phase Change Material - Structural Insulated Panels (PCM -SIPs), In: Civil, Environmental and Architectural Engineering. 2004, University of Kansas: Lawrence.
3. Zhang, M., M. A. Medina, et al. (2005). "Development of a thermally enhanced frame wall with phase change materials for on peak air conditioning demand reduction and energy savings in residential buildings." International journal of energy research 29(9): 795-809.
4. Zhang M. Performance Evaluation of a Phase Change Frame Wall, In: Civil, Environmental and Architectural Engineering. 2004, University of Kansas: Lawrence.
5. Angela C. Evers, Development of a Quantitative Measure of the Functionality of Frame Walls Enhanced with Phase Change Materials Using Dynamic Wall Simulator, In: Civil, Environmental and Architectural Engineering. 2008, University of Kansas: Lawrence.
6. Yuan Fang, A Comprehensive study of Phase Change materials (PCMs) for building walls applications, In: Civil, Environmental and Architectural Engineering. 2009, University of Kansas: Lawrence.
7. Silvia Reshmeen, Determining the Optimum Placement of a Phase Change Materials (PCMs) Thermal Shield Inside Frame Walls Using a Dynamic Wall Simulator, In Civil, Environmental and Architectural Engineering. 2009, University of Kansas: Lawrence.

8. Mashud Ahmed, Energy Consumption in Insulated Refrigerated Trucks and Heat Transfer Reduction by the Application of Phase Change Material-A Passive Cooling Technology, In: Mechanical Engineering. 2009, University of Kansas: Lawrence.
9. Martynov, A. (1976). "The terminology of low-temperature technology (discussion)." Chemical and Petroleum Engineering 12(5): 470-472.
10. Available from <http://explorepahistory.com/cms/pbfiles/Project1/Scheme31/ExplorePAHistory-a0k8h9-a_735.pdf>
11. Office of Freight Management and Operations. Freight Facts and Figures 2007. 2007, U.S. Department of Transportation, Federal Highway Administration.
12. U.S. Department of Energy. "Fossil Fuels,"
13. American Trucking Association. Fuel Facts. 2007 [cited; Available from: http://www.truckline.com/fuelpricecrisis/fuelfacts].
14. U.S. Department of Transportation, Federal Highway Administration, Highway Statistics 1997.
15. Hagen, J.W., D. Minami, B. Mason, and W. Dunton. 1999. "California's Produce Trucking Industry: Characteristics and Important Issues." Center for Agricultural Business, California Agricultural Technology Institute, California State University – Fresno.
16. Food, Fuel, and Freeways: An Iowa perspective on how far food travels, fuel usage, and greenhouse gas emissions, 2001.
17. Davis SC, Diegel SW, Oak Ridge National Laboratory. Transportation Energy Data Book: Edition 26. 2007, U.S. Department of Energy.

18. Mehling, H. and L. F. Cabeza (2008). Heat and cold storage with PCM: an up to date introduction into basics and applications, Springer Verlag.
19. Farid, M. M., A. M. Khudhair, et al. (2004). "A review on phase change energy storage: materials and applications." Energy Conversion and Management 45(9-10): 1597-1615.
20. PCM-Encapsulation, Phase Change Material Products Limited**,** 2009 [Cited; Available from: http://www.pcmproducts.net/Encapsulated_PCMs.htm].
21. Holman M.2001. Gel-coated Microcapsules. US patent 6270836, Frisby Technologies.
22. Available from < http://www.microteklabs.com/>.
23. M. Telkes, Thermal storage for solar heating and cooling, Proceedings of the Workshop on Solar Energy Storage Subsystems for the Heating and Cooling of Buildings, Charlottesville (Virginia, USA), 1975.
24. Zalba, B., J. M. Marin, et al. (2003). "Review on thermal energy storage with phase change: materials, heat transfer analysis and applications." Applied thermal engineering 23(3): 251-283.
25. U.S. National Climatic Data Center, Monthly Station Climate Summaries, 1971–2000.
26. Hall, I.; Prairie, R.; Anderson, H.; Boes, E. (1978). Generation of Typical Meteorological Years for 26 SOLMET Stations. SAND78-1601. Albuquerque, NM: Sandia National Laboratories.
27. Marion, W., Urban, K., User's Manual for TMY2s-Typical Meteorological Years Derived from the 1961–1990 National Solar Radiation Data Base, NREL/TP-463-7668, Golden, CO: National Renewable Energy Laboratory, 1995.
28. Wilcox, S. (2007). National Solar Radiation Database 1991–2005 Update: User's Manual. 472 pp.; NREL Report No. TP-581-41364.

29. NSRDB. 1961- 1990: Typical Meteorological Year 2.

30. NSRDB. 1991- 2005: Typical Meteorological Year 3.

31. Reindl, D., W. Beckman, et al. (1990). "Diffuse fraction correlations." Solar Energy 45(1): 1-7.

32. Duffie, J. A. and W. A. Beckman (2006). Solar engineering of thermal processes, Wiley.

33. Available from <http://education.gsfc.nasa.gov/experimental/July61999siteupdate/inv99Project.Site/Pages/solar.insolation.html>.

34. Williams, David R. (2004-09-01). "Earth Fact Sheet". NASA. Retrieved 2007-03-17.

35. Available from < http://www.grossmont.edu/judd.curran/outline1.htm>.

36. Available from <http://www.weather.gov/os/windchill/index.shtml>.

37. Available from < http://maps.google.com/maps?hl=en&tab=wl>.

38. Rubitherm GmbH. Paraffins – RT-5, 2008 [cited; Available from: http://www.rubitherm.com/english/index.htm].

39. Osczevski, R. and M. Bluestein (2005). "The new wind chill equivalent temperature chart." Bulletin of the American Meteorological Society 86(10): 1453-1458.

40. Available from < http://www.frigoblock.de/start/?lan=eng>.

41. Walton, G.N., Thermal Analysis Research Program- Reference Manual, NBSIR 83-2655, U.S. Department of Commerce, March 1983, Update 1985.